

# **Theoretical and Experimental Study of the Distribution of Capacitive Times**

Baptiste Py<sup>a</sup>, Adeleke Maradesa<sup>a</sup>, Francesco Ciucci<sup>a,b,\*</sup>

<sup>a</sup> Department of Mechanical and Aerospace Engineering, The Hong Kong University of Science and Technology, Hong Kong SAR, China

<sup>b</sup> Chair of Electrode Design for Electrochemical Energy Systems, University of Bayreuth, 95448 Bayreuth, Germany

\*Corresponding author: [francesco.ciucci@uni-bayreuth.de](mailto:francesco.ciucci@uni-bayreuth.de)

Phone: +49 921 55 4941

## Abstract

The distribution of relaxation times (DRT) method is a non-parametric approach for analyzing electrochemical impedance spectroscopy (EIS) data. However, we must be careful when using the DRT method on electrochemical systems with blocking electrodes, such as those encountered in batteries and supercapacitors. This is because at low frequencies the asymptotic behavior of the DRT model cannot capture unbounded impedances. To address this issue, we explore the distribution of capacitive times (DCT), a method that, despite being developed decades ago, is still not widely used. In this work, we detail the theoretical underpinnings of the DCT, deriving DCT-specific analytical formulae based on several standard impedance models. We also draw parallels between DCT and DRT and show how these two methods differ in capturing timescales and peaks, elucidating the scenarios where DCT can serve as a viable alternative should the DRT not be applicable. This article seeks to expand the scope of non-parametric approaches for EIS data analysis, particularly to systems characterized by blocking electrodes.

Keywords: Electrochemical impedance spectroscopy, Distribution of relaxation times, Distribution of capacitive times, Deep neural network, Batteries.

# 1 Introduction

Electrochemical impedance spectroscopy (EIS) is a non-invasive characterization technique widely utilized in fields as diverse as energy science [1], medicine [2], and biology [3]. It is particularly valued for its ability to probe a broad frequency range, from mHz to MHz, and ease of implementation with contemporary workstations [4]. Despite its appeal, interpreting EIS data remains challenging [5]. Usually, equivalent circuits are employed to analyze EIS spectra [6]. However, multiple circuits can fit the data equally well, and, as a result, some of the developed circuits may not have a physical significance [7]. Conversely, while physical models are grounded in principles of physics and chemistry, they are often specific to particular systems, limiting their general applicability [8]. Furthermore, these physical models are typically more challenging to set up and solve [9]. Over the past two decades, the distribution of relaxation times (DRT) model has emerged as a promising alternative to complement and even replace the above-mentioned methods. The DRT approach models EIS spectra as originating from relaxations [10,11]. This implies that the impedance modeled by the DRT,  $Z_{\text{DRT}}(f)$ , is given by [12,13]

$$Z_{\text{DRT}}(f) = i2\pi f L_0 + R_\infty + \int_{-\infty}^{+\infty} \frac{\gamma_{\text{DRT}}(\log \tau)}{1 + i2\pi f \tau} d \log \tau \quad (1)$$

where  $Z_{\text{DRT}}(f)$  is the DRT model impedance at a frequency  $f$ ,  $L_0$  is an inductance,  $R_\infty$  is a resistance,  $\gamma_{\text{DRT}}(\log \tau)$  is the actual DRT, and  $\tau$  is a timescale.

One point to note is that (1) implies that, as  $f$  tends to 0, the impedance tends to a finite real value, namely  $R_\infty + \int_{-\infty}^{+\infty} \gamma_{\text{DRT}}(\log \tau) d \log \tau$ . In other words, the DRT impedance is asymptotically bounded at low frequencies [14,15]. However, this behavior is inconsistent with systems exhibiting blocking boundary conditions at the electrode-electrolyte interface, such as batteries, supercapacitors, *etc.* [16]. In particular, this asymptotic behavior does not apply to

systems modeled by the finite-space or semi-infinite Warburg diffusion [17,18]. As already alluded to above, the DRT model assumes that the linear response to a blip of current is a voltage relaxation [15]. However, this is not the case for blocking electrodes, in which case, if a voltage is applied, the resulting current is a relaxation. Therefore, in such circumstances, the DRT is replaced by another distribution, which is called the distribution of capacitive times (DCT) [19–21]. In the DCT framework, the admittance,  $Y_{\text{DCT}}(f)$ , *i.e.*, the inverse of the impedance, is given by [21,22]<sup>1</sup>

$$Y_{\text{DCT}}(f) = i2\pi f C_0 + G_0 + \int_{-\infty}^{+\infty} \frac{i2\pi f \tau}{1 + i2\pi f \tau} \gamma_{\text{DCT}}(\log \tau) d \log \tau \quad (2)$$

where  $C_0$  is a capacitance,  $G_0$  is the zero-frequency conductance, and  $\gamma_{\text{DCT}}(\log \tau)$  is the DCT.

We note that (2) can be equivalently rewritten as

$$Y_{\text{DCT}}(f) = i2\pi f C_0 + G_\infty - \int_{-\infty}^{+\infty} \frac{\gamma_{\text{DCT}}(\log \tau)}{1 + i2\pi f \tau} d \log \tau \quad (3)$$

with  $G_\infty = G_0 + \int_{-\infty}^{+\infty} \gamma_{\text{DCT}}(\log \tau) d \log \tau$ . More details are given in Section 1.1 of the Supplementary Information, Part 1 (SI1).

Although the DRT has been extensively studied using methods like Tikhonov regularization [24], Gaussian processes [25], and neural networks [26], the DCT method remains largely unexamined. This study aims to highlight the significance of the DCT, outline differences between the DRT and DCT, and demonstrate how the DCT can be used. To chart this path, we first establish the DCT for several standard impedance models and link them to the DRT. Subsequently, we develop a new machine-learning-based approach with two deep neural

---

<sup>1</sup> We note that the DRT model in (1) arises from Voigt circuits, while the DCT model in (2) originates from Maxwell circuits. Specifically, Voigt circuits are characterized by a series arrangement of parallel resistor-capacitor combinations [21,23], whereas Maxwell circuits involve parallel configurations of series resistor-capacitor pairs [21].

networks to deconvolve the DCT. We validate this method using synthetic and actual battery data.

## 2 The Distribution of Capacitive Times of Elementary Circuits

In this section, we derive the theoretical framework required for using the DCT. Specifically, the analytical DCTs for the generalized Warburg element [27], ZARC element [28], Havriliak-Negami (HN) element, which generalizes the ZARC [29], and a circuit consisting of the series combination of a ZARC element and a generalized Warburg element are derived. These formulae are key for calculating parameters using the DCT. The analytical DCTs for the newly developed YARC element and the de Levie model [30] are also presented. Importantly, similarities and differences between the DRT and DCT are highlighted.

The admittance is computed from the DCT,  $\gamma_{\text{DCT}}(\log \tau)$ , using (3). Conversely, as shown in Section 1.2 of SI1, the DCT is computed from the admittance using the following relation [31]:

$$\gamma_{\text{DCT}}(\log \tau) = \frac{1}{\pi} \Im \left( Y \left( \frac{i}{\tau} \right) + Y \left( -\frac{i}{\tau} \right) \right) \quad (4)$$

where  $\Im(\cdot)$  indicates the imaginary part. The analytical formulae for the DCTs are derived in Sections 1.3 and 1.4 of SI1, and validated in Section 1 in the Supplementary Information, Part 2 (SI2), see Figure S1 and Table S1 of SI2.

### 2.1 Generalized Warburg Element

The impedance,  $Z(f; R_{\infty}, A, \alpha)$ , of the generalized Warburg element is given by [27]

$$Z(f; R_{\infty}, A, \alpha) = R_{\infty} + \frac{A}{(i2\pi f)^{\alpha}} \quad (5)$$

where  $A$  is a Warburg coefficient, and  $\alpha$  is the Warburg exponent<sup>2</sup>.

---

<sup>2</sup> For a physical interpretation of the Warburg circuit, the reader can refer to [32].

As demonstrated in Section 1.3 of SI1, the DCT of (5) is given by

$$\gamma_{\text{DCT}}(\log \tau; R_{\infty}, A, \alpha) = \frac{1}{\pi R_{\infty}} \frac{\frac{1}{R_{\infty}} \sin(\pi \alpha) \left(\frac{\tau}{\tau_{\text{W-DCT}}}\right)^{\alpha}}{1 + 2 \cos(\pi \alpha) \left(\frac{\tau}{\tau_{\text{W-DCT}}}\right)^{\alpha} + \left(\frac{\tau}{\tau_{\text{W-DCT}}}\right)^{2\alpha}} \quad (6)$$

where the characteristic timescale  $\tau_{\text{W-DCT}} = \left(\frac{R_{\infty}}{A}\right)^{1/\alpha} = \sqrt[\alpha]{\frac{R_{\infty}}{A}}$  or, in the more commonly used

$(\log \tau, \gamma_{\text{DCT}})$  plane,  $\log \tau_{\text{W-DCT}} = \frac{1}{\alpha} \log \left(\frac{R_{\infty}}{A}\right)$ .

In the  $(\log \tau, \gamma_{\text{DCT}})$  plane, the DCT peak is located at  $\left(\log \tau_{\text{W-DCT}}, \frac{1}{2\pi R_{\infty}} \tan\left(\frac{\pi \alpha}{2}\right)\right)$ , and its full-width-at-half-maximum value,  $\text{FWHM}_{\log \tau}$ , is given by

$$\text{FWHM}_{\log \tau} = \frac{1}{\alpha} \log \left( \frac{2 \cos\left(\frac{\pi \alpha}{2}\right) \left(\cos\left(\frac{\pi \alpha}{2}\right) + \sqrt{1 + \left(\cos\left(\frac{\pi \alpha}{2}\right)\right)^2}\right) + 1}{2 \cos\left(\frac{\pi \alpha}{2}\right) \left(\cos\left(\frac{\pi \alpha}{2}\right) - \sqrt{1 + \left(\cos\left(\frac{\pi \alpha}{2}\right)\right)^2}\right) + 1} \right) \quad (7)$$

Incidentally, we note that  $\text{FWHM}_{\log \tau}$  decreases as  $\alpha$  increases, see Figure S2 of SI2, implying that as the Warburg line angle increases from 0 to 90 degrees, the  $\text{FWHM}_{\log \tau}$  narrows from  $+\infty$  to 0.

The (6) can be generalized in the case of a circuit comprising a finite collection of series Warburg elements, whose impedance and DCT are given by

$$Z(f; R_{\infty}, \mathbf{A}, \boldsymbol{\alpha}) = R_{\infty} + \sum_{k=1}^K \frac{A_k}{(i2\pi f)^{\alpha_k}} \quad (8a)$$

$$\gamma_{\text{DCT}}(\log \tau; R_{\infty}, \mathbf{A}, \boldsymbol{\alpha}) \quad (8b)$$

$$= \frac{1}{\pi} \frac{\sum_{k=1}^K A_k \sin(\pi \alpha_k) \tau^{\alpha_k}}{(R_{\infty} + \sum_{k=1}^K A_k \cos(\pi \alpha_k) \tau^{\alpha_k})^2 + (\sum_{k=1}^K A_k \sin(\pi \alpha_k) \tau^{\alpha_k})^2}$$

with  $\mathbf{A} = (A_1, A_2, \dots, A_K)^{\top}$ ,  $\boldsymbol{\alpha} = (\alpha_1, \alpha_2, \dots, \alpha_K)^{\top}$ , where, for  $k = 1, 2, \dots, K$ ,  $A_k$  and  $\alpha_k$  are the  $k$ -th Warburg coefficient and Warburg exponent, respectively.

## 2.2 ZARC Element

The ZARC element is widely used in electrochemistry [33], and its impedance,  $Z(f; R_\infty, R_{ct}, \tau_{ZARC}, \phi)$  is given by [28]

$$Z(f; R_\infty, R_{ct}, \tau_{ZARC}, \phi) = R_\infty + \frac{R_{ct}}{1 + (i2\pi f \tau_{ZARC})^\phi} \quad (9)$$

where  $R_{ct}$ ,  $\tau_{ZARC}$ , and  $\phi$  are a resistance, a timescale, and a dispersion parameter, respectively.

The DRT,  $\gamma_{DRT}(\log \tau; R_{ct}, \tau_{ZARC}, \phi)$ , is given by (further details are given in Section 1.3 of SI1)

$$\gamma_{DRT}(\log \tau; R_{ct}, \tau_{ZARC}, \phi) = \frac{1}{\pi} \frac{R_{ct} \sin(\pi\phi) \left(\frac{\tau}{\tau_{ZARC}}\right)^\phi}{1 + 2 \cos(\pi\phi) \left(\frac{\tau}{\tau_{ZARC}}\right)^\phi + \left(\frac{\tau}{\tau_{ZARC}}\right)^{2\phi}} \quad (10)$$

while the DCT,  $\gamma_{DCT}(\log \tau; R_\infty, R_{ct}, \tau_{ZARC}, \phi)$ , is given by

$$\gamma_{DCT}(\log \tau; R_{ct}, \tau_{ZARC}, \phi) = \frac{1}{\pi} \frac{\frac{1}{R_{ZARC-DCT}} \sin(\pi\phi) \left(\frac{\tau}{\tau_{ZARC-DCT}}\right)^\phi}{1 + 2 \cos(\pi\phi) \left(\frac{\tau}{\tau_{ZARC-DCT}}\right)^\phi + \left(\frac{\tau}{\tau_{ZARC-DCT}}\right)^{2\phi}} \quad (11)$$

with  $R_{ZARC-DCT} = \frac{R_\infty(R_\infty + R_{ct})}{R_{ct}}$  and  $\tau_{ZARC-DCT} = \tau_{ZARC} \left(\frac{R_\infty}{R_\infty + R_{ct}}\right)^{\frac{1}{\phi}}$ . The DCT peak timescale is

lower than the ZARC timescale by the factor  $\left(\frac{R_\infty}{R_\infty + R_{ct}}\right)^{\frac{1}{\phi}}$ , assuming  $0 < \phi < 1$ . This is unsurprising since the DRT is related to the voltage relaxation following a current step, while the DCT arises from the current relaxation after a voltage blip (Section 1).

We emphasize that (10) and (11) underpin similar expressions since

$$\gamma_{DCT}(\log \tau; R_{ct}, \tau_{ZARC}, \phi) = \gamma_{DRT}\left(\log \tau; \frac{1}{R_{ZARC-DCT}}, \tau_{ZARC-DCT}, \phi\right) . \quad \text{Furthermore, the}$$

$\text{FWHM}_{\log \tau}$  of the Warburg DCT and the ZARC DCT (see (7)) are identical provided that  $\phi = \alpha$ . More details are given in Section 5.1.2.

The ZARC element is a particular case of the HN element, whose impedance,  $Z(f; R_\infty, R_{\text{ct}}, \tau_{\text{HN}}, \phi, \psi)$ , can be written as follows [34]:

$$Z(f; R_\infty, R_{\text{ct}}, \tau_{\text{HN}}, \phi, \psi) = R_\infty + \frac{R_{\text{ct}}}{(1 + (i2\pi f \tau_{\text{ZARC}})^\phi)^\psi} \quad (12)$$

where  $\psi$  is a symmetry parameter between 0 and 1 [35]. The HN impedance reduces to the ZARC impedance for  $\psi = 1$ . It follows that (11) is a particular case of the HN DCT,  $\gamma_{\text{DCT}}(\log \tau; R_\infty, R_{\text{ct}}, \tau_{\text{HN}}, \phi, \psi)$ , (the derivation can be found in Section 1.3 of SI1) which is given by

$$\gamma_{\text{DCT}}(\log \tau; R_\infty, R_{\text{ct}}, \tau_{\text{HN}}, \phi, \psi) = \frac{1}{\pi} \frac{\tilde{R}_{\text{ct}} \sin(\psi\theta)}{(R_\infty + \tilde{R}_{\text{ct}} \cos(\psi\theta))^2 + (\tilde{R}_{\text{ct}} \sin(\psi\theta))^2} \quad (13)$$

In the latter equation, the quantities  $\tilde{R}_{\text{ct}}$  and  $\theta$  are defined as

$$\tilde{R}_{\text{ct}} = R_{\text{ct}} \frac{\left(\frac{\tau}{\tau_{\text{HN}}}\right)^{\psi\phi}}{\left(1 + 2 \cos(\pi\phi) \left(\frac{\tau}{\tau_{\text{HN}}}\right)^\phi + \left(\frac{\tau}{\tau_{\text{HN}}}\right)^{2\phi}\right)^{\frac{\psi}{2}}} \quad (14a)$$

$$\theta = \begin{cases} \arctan\left(\frac{\sin(\pi\phi)}{\left(\frac{\tau}{\tau_{\text{HN}}}\right)^\phi + \cos(\pi\phi)}\right) & \text{if } \frac{\sin(\pi\phi)}{\left(\frac{\tau}{\tau_{\text{HN}}}\right)^\phi + \cos(\pi\phi)} \geq 0 \\ \pi + \arctan\left(\frac{\sin(\pi\phi)}{\left(\frac{\tau}{\tau_{\text{HN}}}\right)^\phi + \cos(\pi\phi)}\right) & \text{if } \frac{\sin(\pi\phi)}{\left(\frac{\tau}{\tau_{\text{HN}}}\right)^\phi + \cos(\pi\phi)} < 0 \end{cases} \quad (14b)$$

As demonstrated in Section 1.3 of SI1, (13) can be generalized in the case of a circuit comprising a finite collection of series HN elements. Specifically, the generalized impedance and DCT are given by

$$Z(f; R_\infty, \mathbf{R}_{\text{ct}}, \boldsymbol{\tau}_{\text{HN}}, \boldsymbol{\phi}, \psi) = R_\infty + \sum_{k=1}^K \frac{R_{\text{ct},k}}{\left(1 + (i2\pi f \tau_{\text{HN},k})^{\phi_k}\right)^{\psi_k}} \quad (15a)$$



$$\gamma_{\text{DCT}}(\log \tau; R_\infty, \mathbf{R}_{\text{ct}}, \boldsymbol{\tau}_{\text{HN}}, \boldsymbol{\phi}, \boldsymbol{\psi}) \quad (15b)$$

$$= \frac{1}{\pi} \frac{\sum_{k=1}^K \tilde{R}_{\text{ct},k} \sin(\psi_k \theta_k)}{\left(R_\infty + \sum_{k=1}^K \tilde{R}_{\text{ct},k} \cos(\psi_k \theta_k)\right)^2 + \left(\sum_{k=1}^K \tilde{R}_{\text{ct},k} \sin(\psi_k \theta_k)\right)^2}$$

where  $\mathbf{R}_{\text{ct}} = (R_{\text{ct},1}, R_{\text{ct},2}, \dots, R_{\text{ct},K})^\top$ ,  $\boldsymbol{\tau}_{\text{HN}} = (\tau_{\text{HN},1}, \tau_{\text{HN},2}, \dots, \tau_{\text{HN},K})^\top$ ,  $\boldsymbol{\phi} = (\phi_1, \phi_2, \dots, \phi_K)^\top$ ,  $\boldsymbol{\psi} = (\psi_1, \psi_2, \dots, \psi_K)^\top$ , and for  $k = 1, 2, \dots, K$   $R_{\text{ct},k}$ ,  $\tau_{\text{HN},k}$ ,  $\phi_k$ , and  $\psi_k$  are the  $k$ -th resistance, timescale, dispersion parameter, and symmetry parameter, respectively. In (15), the quantities  $\tilde{R}_{\text{ct},k}$  and  $\theta_k$  are defined for  $k = 1, 2, \dots, K$  as

$$\tilde{R}_{\text{ct},k} = R_{\text{ct},k} \frac{\left(\frac{\tau}{\tau_{\text{HN},k}}\right)^{\psi_k \phi_k}}{\left(1 + 2 \cos(\pi \phi_k) \left(\frac{\tau}{\tau_{\text{HN},k}}\right)^{\phi_k} + \left(\frac{\tau}{\tau_{\text{HN},k}}\right)^{2\phi_k}\right)^{\frac{\psi_k}{2}}} \quad (16a)$$

$$\theta_k = \begin{cases} \arctan\left(\frac{\sin(\pi \phi_k)}{\left(\frac{\tau}{\tau_{\text{HN},k}}\right)^{\phi_k} + \cos(\pi \phi_k)}\right) & \text{if } \frac{\sin(\pi \phi_k)}{\left(\frac{\tau}{\tau_{\text{HN},k}}\right)^{\phi_k} + \cos(\pi \phi_k)} \geq 0 \\ \pi + \arctan\left(\frac{\sin(\pi \phi_k)}{\left(\frac{\tau}{\tau_{\text{HN},k}}\right)^{\phi_k} + \cos(\pi \phi_k)}\right) & \text{if } \frac{\sin(\pi \phi_k)}{\left(\frac{\tau}{\tau_{\text{HN},k}}\right)^{\phi_k} + \cos(\pi \phi_k)} < 0 \end{cases} \quad (16b)$$

We stress that setting  $\psi_1 = \psi_2 = \dots = \psi_K = 1$  in (15b) gives the generalized DCT of a series circuit comprising a finite collection of ZARC elements (see Section 5.2.1.1).

### 2.3 ZARC + Generalized Warburg

The impedance of the series combination of a ZARC element (Section 2.2) and a generalized Warburg element (Section 2.1) is given by

$$Z(f; R_\infty, R_{\text{ct}}, \tau_{\text{ZARC}}, \phi, A, \alpha) = R_\infty + \frac{R_{\text{ct}}}{1 + (i2\pi f \tau_{\text{ZARC}})^\phi} + \frac{A}{(i2\pi f)^\alpha} \quad (17)$$

Given that the ZARC and Warburg timescales are separated with the ZARC timescale being much lower than the Warburg timescale, the admittance,  $Y(f; R_\infty, R_{ct}, \tau_{ZARC}, \phi, A, \alpha)$ , can be approximated as

$$Y(f; R_\infty, R_{ct}, \tau_{ZARC}, \phi, A, \alpha) \approx \frac{1}{R_\infty + \frac{R_{ct}}{1 + (i2\pi f \tau_{ZARC})^\phi}} + \frac{1}{R_\infty + R_{ct} + \frac{A}{(i2\pi f)^\alpha}} \quad (18)$$

As detailed in Section 1.3 of SI1, the DCT,  $\gamma_{DCT}(\log \tau; R_\infty, R_{ct}, \tau_{ZARC}, \phi, A, \alpha)$ , can be approximated as

$$\gamma_{DCT}(\log \tau; R_\infty, R_{ct}, \tau_{ZARC}, \phi, A, \alpha) \quad (19)$$

$$\begin{aligned} & \approx \frac{1}{\pi} \frac{\frac{1}{R_{ZARC-DCT}} \sin(\pi\phi) \left(\frac{\tau}{\tau_{ZARC-DCT}}\right)^\phi}{1 + 2 \cos(\pi\phi) \left(\frac{\tau}{\tau_{ZARC-DCT}}\right)^\phi + \left(\frac{\tau}{\tau_{ZARC-DCT}}\right)^{2\phi}} \\ & + \frac{1}{\pi} \frac{\frac{1}{R_\infty + R_{ct}} \sin(\pi\alpha) \left(\frac{\tau}{\tau_{W-DCT}}\right)^\alpha}{1 + 2 \cos(\pi\alpha) \left(\frac{\tau}{\tau_{W-DCT}}\right)^\alpha + \left(\frac{\tau}{\tau_{W-DCT}}\right)^{2\alpha}} \end{aligned}$$

with  $R_{ZARC-DCT} = \frac{R_\infty(R_\infty + R_{ct})}{R_{ct}}$ ,  $\tau_{ZARC-DCT} = \tau_{ZARC} \left(\frac{R_\infty}{R_\infty + R_{ct}}\right)^{\frac{1}{\phi}}$ , and  $\tau_{W-DCT} = \left(\frac{R_\infty + R_{ct}}{A}\right)^{\frac{1}{\alpha}}$ .

We stress that the position,  $\log \tau_{ZARC-DCT}$ , of the DCT peak in the  $(\log \tau, \gamma_{DCT})$  space for the ZARC element remains unchanged. However, the position,  $\log \tau_{W-DCT} = \frac{1}{\alpha} \log \left(\frac{R_\infty + R_{ct}}{A}\right)$ , of the DCT peak for the generalized Warburg element is shifted and depends on  $R_{ct}$ .

Moreover, (8b) and (15b) can be generalized to the series circuit comprising a finite collection of HN elements and generalized Warburg elements (Section 1.3 of SI1). Specifically, the generalized impedance and DCT are given by

$$Z(f; R_\infty, \mathbf{R}_{\text{ct}}, \boldsymbol{\tau}_{\text{HN}}, \boldsymbol{\phi}, \boldsymbol{\psi}, \mathbf{A}, \boldsymbol{\alpha}) = R_\infty + \sum_{k=1}^K \frac{R_{\text{ct},k}}{\left(1 + (i2\pi f \tau_{\text{HN},k})^{\phi_k}\right)^{\psi_k}} + \sum_{p=1}^P \frac{A_p}{(i2\pi f)^{\alpha_p}} \quad (20a)$$

$$\gamma_{\text{DCT}}(\log \tau; R_\infty, \mathbf{R}_{\text{ct}}, \boldsymbol{\tau}_{\text{HN}}, \boldsymbol{\phi}, \boldsymbol{\psi}, \mathbf{A}, \boldsymbol{\alpha}) \quad (20b)$$

$$= \frac{1}{\pi} \frac{\sum_{k=1}^K \tilde{R}_{\text{ct},k} \sin(\psi_k \theta_k) + \sum_{p=1}^P A_p \sin(\pi \alpha_p) \tau^{\alpha_p}}{\left(R_\infty + \sum_{k=1}^K \tilde{R}_{\text{ct},k} \cos(\psi_k \theta_k) + \sum_{p=1}^P A_p \cos(\pi \alpha_p) \tau^{\alpha_p}\right)^2 + \left(\sum_{k=1}^K \tilde{R}_{\text{ct},k} \sin(\psi_k \theta_k) + \sum_{p=1}^P A_p \sin(\pi \alpha_p) \tau^{\alpha_p}\right)^2}$$

where we recall that  $\mathbf{R}_{\text{ct}} = (R_{\text{ct},1}, R_{\text{ct},2}, \dots, R_{\text{ct},K})^\top$ ,  $\boldsymbol{\tau}_{\text{HN}} = (\tau_{\text{HN},1}, \tau_{\text{HN},2}, \dots, \tau_{\text{HN},K})^\top$ ,  $\boldsymbol{\phi} = (\phi_1, \phi_2, \dots, \phi_K)^\top$ ,  $\boldsymbol{\psi} = (\psi_1, \psi_2, \dots, \psi_K)^\top$ ,  $\mathbf{A} = (A_1, A_2, \dots, A_P)^\top$ , and  $\boldsymbol{\alpha} = (\alpha_1, \alpha_2, \dots, \alpha_P)^\top$ , and the parameters  $\tilde{R}_{\text{ct},k}$  and  $\theta_k$  for  $k = 1, 2, \dots, K$  are defined in (16).

We note that setting  $\psi_1 = \psi_2 = \dots = \psi_K = 1$  in (20b) gives the generalized DCT of a circuit comprising a finite collection of ZARC elements and generalized Warburg elements in series (Section 1.3 of SI1).

## 2.4 YARC Element

As discussed in Section 2.2, the analytical DRT and DCT of the ZARC element are formally identical. Therefore, we propose the new YARC element whose admittance is given by

$$Y(f; G_\infty, G_{\text{ct}}, \tau_{\text{YARC}}, \phi) = G_\infty + G_{\text{ct}} - \frac{G_{\text{ct}}}{1 + (i2\pi f \tau_{\text{YARC}})^\phi} \quad (21)$$

where  $G_{\text{ct}}$  is a conductance, and  $\tau_{\text{YARC}}$  is a timescale.

The DCT,  $\gamma_{\text{DCT}}(\log \tau; G_{\text{ct}}, \tau_{\text{YARC}}, \phi)$ , of the YARC element is such that  $\gamma_{\text{DCT}}(\log \tau; G_{\text{ct}}, \tau_{\text{YARC}}, \phi) = \gamma_{\text{DRT}}(\log \tau; R_{\text{ct}}, \tau_{\text{ZARC}}, \phi)$  with  $\gamma_{\text{DRT}}(\log \tau; R_{\text{ct}}, \tau_{\text{ZARC}}, \phi)$  the DRT of the ZARC element given in (10), *i.e.*, (the derivation is given in Section 1.3 of SI1)

$$\gamma_{\text{DCT}}(\log \tau; G_{\text{ct}}, \tau_{\text{YARC}}, \phi) = \frac{1}{\pi} \frac{G_{\text{ct}} \sin(\pi\phi) \left(\frac{\tau}{\tau_{\text{YARC}}}\right)^\phi}{1 + 2 \cos(\pi\phi) \left(\frac{\tau}{\tau_{\text{YARC}}}\right)^\phi + \left(\frac{\tau}{\tau_{\text{YARC}}}\right)^{2\phi}} \quad (22)$$

We note that (22) can be generalized as

$$\gamma_{\text{DCT}}(\log \tau; G_{\text{ct}}, \tau_{\text{YARC}}, \phi, \psi) = \frac{1}{\pi} \frac{G_{\text{ct}} \sin(\psi\theta) \left(\frac{\tau}{\tau_{\text{YARC}}}\right)^{\phi\psi}}{\left(1 + 2 \cos(\pi\phi) \left(\frac{\tau}{\tau_{\text{YARC}}}\right)^\phi + \left(\frac{\tau}{\tau_{\text{YARC}}}\right)^{2\phi}\right)^{\frac{\psi}{2}}} \quad (23)$$

where  $\theta = \arctan\left(\left|\frac{\sin(\pi\phi)}{\left(\frac{\tau}{\tau_{\text{YARC}}}\right)^\phi + \cos(\pi\phi)}\right|\right)$ .

Moreover, (22) can be easily generalized to the parallel combination of multiple YARC elements. Specifically, their admittance and DCT are given (respectively) by

$$Y(f; G_\infty, \mathbf{G}_{\text{ct}}, \boldsymbol{\tau}_{\text{YARC}}, \boldsymbol{\phi}) = G_\infty + \sum_{k=1}^K G_{\text{ct},k} - \sum_{k=1}^K \frac{G_{\text{ct},k}}{1 + (i2\pi f \tau_{\text{YARC},k})^{\phi_k}} \quad (24a)$$

$$\gamma_{\text{DCT}}(\log \tau; \mathbf{G}_{\text{ct}}, \boldsymbol{\tau}_{\text{YARC}}, \boldsymbol{\phi}) = \frac{1}{\pi} \sum_{k=1}^K \frac{G_{\text{ct},k} \sin(\pi \phi_k) \left( \frac{\tau}{\tau_{\text{YARC},k}} \right)^{\phi_k}}{1 + 2 \cos(\pi \phi_k) \left( \frac{\tau}{\tau_{\text{YARC},k}} \right)^{\phi_1} + \left( \frac{\tau}{\tau_{\text{YARC},k}} \right)^{2\phi_k}} \quad (24b)$$

where  $\mathbf{G}_{\text{ct}} = (G_{\text{ct},1}, G_{\text{ct},2}, \dots, G_{\text{ct},K})^\top$  and  $\boldsymbol{\tau}_{\text{YARC}} = (\tau_{\text{YARC},1}, \tau_{\text{YARC},2}, \dots, \tau_{\text{YARC},K})^\top$ , and for  $k = 1, 2, \dots, K$   $G_{\text{ct},k}$  and  $\tau_{\text{YARC},k}$  are the  $k$ -th conductance and timescale, respectively.

## 2.5 De Levie's Model

De Levie's model was developed to describe the impedance of porous electrodes [30,36]. Assuming that the pores are cylindrical, only the sides of the pores are conducting, and that there is no radial ac gradient, the electrode impedance is given by

$$Z(f; R_\infty, R_{\text{ion}}, R_{\text{ct}}, \tau_0, \phi) = R_\infty + \sqrt{R_{\text{ion}} Z_0(f; R_{\text{ct}}, \tau_0, \phi)} \coth \left( \sqrt{\frac{R_{\text{ion}}}{Z_0(f; R_{\text{ct}}, \tau_0, \phi)}} \right) \quad (25)$$

where  $Z_0(f; R_{\text{ct}}, \tau_0, \phi) = \frac{R_{\text{ct}}}{1 + (i2\pi f \tau_0)^\phi}$ , and  $R_\infty$ ,  $R_{\text{ion}}$ ,  $R_{\text{ct}}$ ,  $\tau_0$ , and  $\phi$  are the resistance of the solution outside the pores, the ionic resistance, the charge-transfer resistance, a characteristic timescale, and a dispersion parameter, respectively [16,37].

The DCT of this impedance model (see Section 1.4 of SI1 for the derivation) is obtained as

$$\begin{aligned} \gamma_{\text{DCT}}(\log \tau; R_\infty, R_{\text{ion}}, R_{\text{ct}}, \tau_0, \phi) &= \left( \frac{\sqrt{R_{\text{ion}} \tilde{R}_{\text{ct}}} (x \sin(2\beta y) + y \sinh(2\beta x))}{2\pi((\sin(\beta y))^2 + (\sinh(\beta x))^2)} \right) \left[ (R_\infty)^2 \right. \\ &+ \frac{\sqrt{R_{\text{ion}} \tilde{R}_{\text{ct}}} R_\infty (x \sinh(2\beta x) - y \sin(2\beta y))}{((\sin(\beta y))^2 + (\sinh(\beta x))^2)} \\ &\left. + \frac{R_{\text{ion}} \tilde{R}_{\text{ct}} ((\sinh(2\beta x))^2 + (\sin(2\beta y))^2)}{4((\sin(\beta y))^2 + (\sinh(\beta x))^2)^2} \right]^{-1} \end{aligned} \quad (26)$$

In the latter equation, the parameters  $\tilde{R}_{\text{ct}}$ ,  $x$ ,  $y$ ,  $\beta$  are defined as

$$\tilde{R}_{\text{ct}} = R_{\text{ct}} \frac{\left(\frac{\tau}{\tau_0}\right)^\phi}{\sqrt{1 + 2 \cos(\pi\phi) \left(\frac{\tau}{\tau_0}\right)^\phi + \left(\frac{\tau}{\tau_0}\right)^{2\phi}}} \quad (27a)$$

$$\begin{cases} x = \cos\left(\frac{\theta}{2}\right) \\ y = \sin\left(\frac{\theta}{2}\right) \end{cases} \quad (27b)$$

$$\theta = \begin{cases} \arctan\left(\frac{\sin(\pi\phi)}{\left(\frac{\tau}{\tau_0}\right)^\phi + \cos(\pi\phi)}\right) & \text{if } \frac{\sin(\pi\phi)}{\left(\frac{\tau}{\tau_0}\right)^\phi + \cos(\pi\phi)} \geq 0 \\ \pi + \arctan\left(\frac{\sin(\pi\phi)}{\left(\frac{\tau}{\tau_0}\right)^\phi + \cos(\pi\phi)}\right) & \text{if } \frac{\sin(\pi\phi)}{\left(\frac{\tau}{\tau_0}\right)^\phi + \cos(\pi\phi)} < 0 \end{cases} \quad (27c)$$

$$\beta = \sqrt{\frac{R_{\text{ion}}}{\tilde{R}_{\text{ct}}}} \quad (27d)$$

### 3 Distribution of Capacitive Times Inverse Problem

Given a set of EIS frequencies,  $\mathbf{f} = (f_1, f_2, \dots, f_M)^\top$ , and a set of equispaced log timescales,  $\log \boldsymbol{\tau} = (\log \tau_1, \log \tau_2, \dots, \log \tau_N)^\top$ , we discretized (3) as

$$\mathbf{Y}_{\text{DCT}}(\mathbf{f}) = G_\infty \mathbf{1} + C_0 i 2\pi \mathbf{f} + \left( \mathbf{A}_{\text{re,DCT}}(\log \boldsymbol{\tau}, \mathbf{f}) + i \mathbf{A}_{\text{im,DCT}}(\log \boldsymbol{\tau}, \mathbf{f}) \right) \boldsymbol{\gamma}_{\text{DCT}}(\log \boldsymbol{\tau}) \quad (28)$$

where  $\mathbf{Y}_{\text{DCT}}(\mathbf{f}) = (Y_{\text{DCT}}(f_1), Y_{\text{DCT}}(f_2), \dots, Y_{\text{DCT}}(f_M))^\top$  is the vector of discretized admittances,  $\mathbf{1}$  is the vector of  $M$  ones,  $\boldsymbol{\gamma}_{\text{DCT}}(\log \boldsymbol{\tau}) = (\gamma_{\text{DCT}}(\log \tau_1), \gamma_{\text{DCT}}(\log \tau_2), \dots, \gamma_{\text{DCT}}(\log \tau_N))^\top$  is the discretized DCT vector, and the two matrices  $\mathbf{A}_{\text{re,DCT}}(\log \boldsymbol{\tau}, \mathbf{f})$  and  $\mathbf{A}_{\text{im,DCT}}(\log \boldsymbol{\tau}, \mathbf{f})$  are based on our previous work [38] (further details are provided in Section 1.5 of SI1).

Herein, we used two feedforward deep neural networks (DNNs). The first network, denoted as GC-DNN, takes a vector identifying experimental conditions, such as temperature and pressure, and generically indicated as  $\boldsymbol{\psi}$ , to return the model parameters  $C_0$  and  $G_\infty$  (given (3)). A second

DNN, called  $\gamma_{\text{DCT}}$ -DNN, takes the vector of experimental conditions and the specific log timescale considered,  $\log \tau$ , to output the DCT.  $\gamma_{\text{DCT}}$ -DNN can be ultimately understood as a generic function with inputs  $\boldsymbol{\psi}$  and  $\log \boldsymbol{\tau}$ . Both DNNs are simple feedforward dense neural networks with five layers, including one input layer, three hidden layers, and one output layer. The dimensions of the input, hidden, and output layers of the GC-DNN are  $\dim(\boldsymbol{\psi})$ , the dimension of the experimental state  $\boldsymbol{\psi}$ , 10, and 2, respectively. For the  $\gamma_{\text{DCT}}$ -DNN, the dimensions of the input, hidden, and output layers are  $\dim(\boldsymbol{\psi}) + 1$  (where the +1 comes from  $\log \tau$ ), 50, and 1, respectively. As shown in our recent works [26,39], pretraining enables us to significantly reduce the training time. Therefore, we pretrained the DNNs using the DCT obtained from ridge regression with the pyDRTtools<sup>3</sup>. For both DNNs, the weights and biases were initialized with Xavier uniform method [40] and to zero, respectively. Furthermore, the input and hidden layers of both DNNs were equipped with non-saturating exponential linear units [41], while the softplus activation function was used at the DNNs output layer to enforce the non-negativity constraint on the DCT [42]. Additionally, we used the following loss function to train the DNN:

$$\begin{aligned}
\mathcal{L} \left( G_{0,\text{DNN}}(\boldsymbol{\psi}), C_{0,\text{DNN}}(\boldsymbol{\psi}), \boldsymbol{\gamma}_{\text{DNN}}(\log \boldsymbol{\tau}, \boldsymbol{\psi}) \right) & \quad (29) \\
= & \left\| \boldsymbol{Y}_{\text{exp}}(\boldsymbol{f}, \boldsymbol{\psi}) - G_0 \mathbf{1} - C_0 i 2\pi \boldsymbol{f} \right. \\
& \left. - \left( \mathbf{A}_{\text{re,DCT}}(\log \boldsymbol{\tau}, \boldsymbol{f}) + i \mathbf{A}_{\text{im,DCT}}(\log \boldsymbol{\tau}, \boldsymbol{f}) \right) \boldsymbol{\gamma}_{\text{DNN}}(\log \boldsymbol{\tau}, \boldsymbol{\psi}) \right\|^2 \\
& + \left( G_{0,\text{RR}}(\boldsymbol{\psi}) - G_{0,\text{DNN}}(\boldsymbol{\psi}) \right)^2 + \left( C_{0,\text{RR}}(\boldsymbol{\psi}) - C_{0,\text{DNN}}(\boldsymbol{\psi}) \right)^2 \\
& + \left\| \boldsymbol{\gamma}_{\text{RR}}(\log \boldsymbol{\tau}, \boldsymbol{\psi}) - \boldsymbol{\gamma}_{\text{DNN}}(\log \boldsymbol{\tau}, \boldsymbol{\psi}) \right\|^2
\end{aligned}$$

---

<sup>3</sup> To deconvolve the DCT with the pyDRTtools, we discretized the integral in (2) with piecewise-linear functions, used the second derivative for the penalty in ridge regression, set the regularization parameter to  $10^{-3}$ , considered the full admittance spectrum, and excluded the capacitance,  $C_0$  [24,38].

where  $G_{0,\text{DNN}}(\boldsymbol{\psi})$ ,  $C_{0,\text{DNN}}(\boldsymbol{\psi})$ , and  $\boldsymbol{\gamma}_{\text{DNN}}(\log \boldsymbol{\tau}, \boldsymbol{\psi})$  are the conductance, capacitance, and DCT outputted by the DNN, respectively,  $\|\cdot\|$  is the Euclidian norm,  $\mathbf{Y}_{\text{exp}}(\mathbf{f}, \boldsymbol{\psi}) = (Y_{\text{exp}}(f_1, \boldsymbol{\psi}), Y_{\text{exp}}(f_2, \boldsymbol{\psi}), \dots, Y_{\text{exp}}(f_M, \boldsymbol{\psi}))^\top$  is the vector of experimental admittances, and  $G_{0,\text{RR}}(\boldsymbol{\psi})$ ,  $C_{0,\text{RR}}(\boldsymbol{\psi})$ , and  $\boldsymbol{\gamma}_{\text{RR}}(\log \boldsymbol{\tau}, \boldsymbol{\psi})$  are the conductance, capacitance, and DCT obtained by ridge regression using the pyDRTtools, respectively.

The Adam algorithm [43] was used with a learning rate of  $10^{-5}$  to minimize  $\mathcal{L}(G_{0,\text{DNN}}(\boldsymbol{\psi}), C_{0,\text{DNN}}(\boldsymbol{\psi}), \boldsymbol{\gamma}_{\text{DNN}}(\log \boldsymbol{\tau}, \boldsymbol{\psi}))$  in (29) [34]. Unless otherwise specified, the maximum number of iterations was set to  $1.00 \times 10^5$ . When needed, DCT peaks were separated using a modification of peak-separation algorithm available in pyDRTtools (Sections 5.2.1.1 and 5.2.1.3) [24,38], and the DCT was integrated with the trapezoidal rule (Section 5.2.1.3).

## 4 Generation of Artificial Experiments

To test the robustness of the DNN approach, we first used artificial EIS data,  $Z_{\text{exp}}(f)$ , generated by imposing synthetic noise,  $\varepsilon(f)$ , to an exact impedance,  $Z_{\text{exact}}(f)$ , *i.e.*,

$$Z_{\text{exp}}(f) = Z_{\text{exact}}(f) + \varepsilon(f) \quad (30)$$

Unless otherwise specified, the frequencies ranged from  $10^{-2}$  Hz to  $10^6$  Hz with 10 points per decade, and we assumed  $\varepsilon(f) \sim \sigma_n^{\text{exp}} \mathcal{N}(0,1)$  with  $\sigma_n^{\text{exp}} = 5.00 \times 10^{-1} \Omega$  [24,44].

## 5 Results

In this section, we first show how to interpret DCT spectra of several elementary circuits. Next, we deconvolve the DCT of artificial and real battery data to highlight the usefulness of the DCT method when the DRT cannot be used. We also show how to compute physical parameters using the DCT.



## 5.1 Comparison of the Distributions of Capacitive and Relaxation Times

### 5.1.1 Generalized Warburg Element

We start with the generalized Warburg element (Section 2.1). The values of the parameters used are reported in Table S2 of SI2. Panels (a), (b), and (c) of Figure 1 show the Nyquist plots of the impedance, admittance, and the DCT plots obtained for different values of the Warburg exponent  $\alpha$ , respectively.

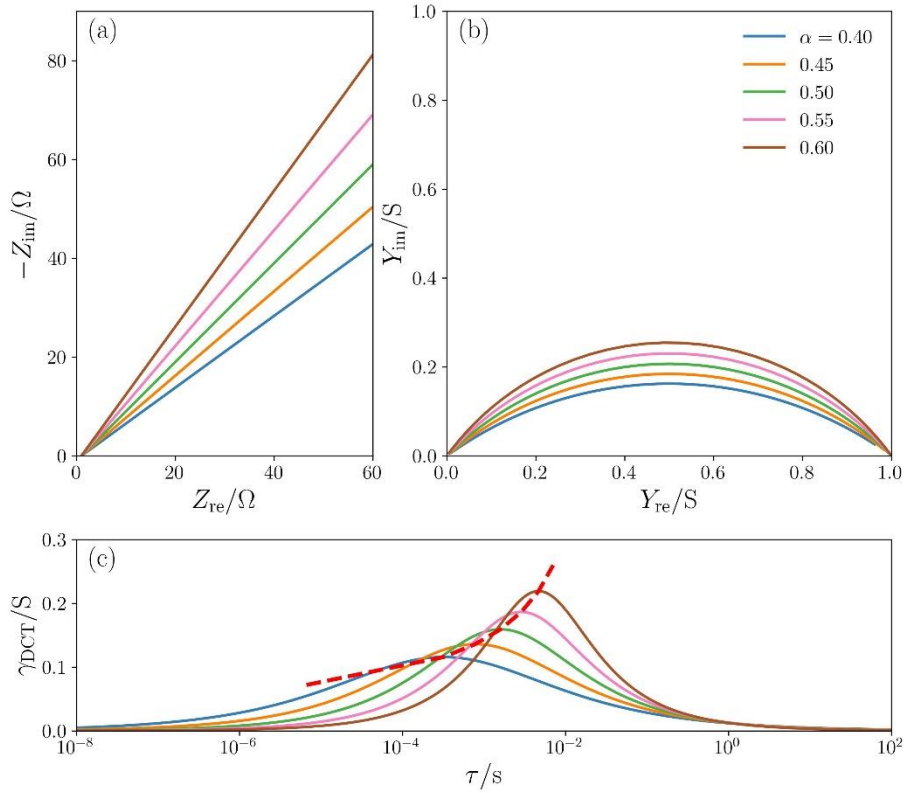


Figure 1. Nyquist plots of the (a) impedance and (b) admittance, and (c) DCT for the generalized Warburg element at various  $\alpha$  values.

When the Warburg exponent  $\alpha$  increases, the DCT peak position,  $\log \tau_{W-DCT} = \frac{1}{\alpha} \log \left( \frac{R_{\infty}}{A} \right)$ , is shifted to higher timescales, the peak height,  $\frac{1}{2\pi R_{\infty}} \tan \left( \frac{\pi\alpha}{2} \right)$ , increases, and the spread,  $FWHM_{\log \tau}$ , decreases, as shown in Figure 1 (c) and Figure S2 of SI2. Panels (a), (b), and (c) of Figure 2 show the impedance, admittance, and DCT, respectively, for various  $R_{\infty}$  values.

We note that an increase in  $R_\infty$  increases  $\log \tau_{W-DCT}$  while decreasing the peak height and area (Figure 2 (c)).

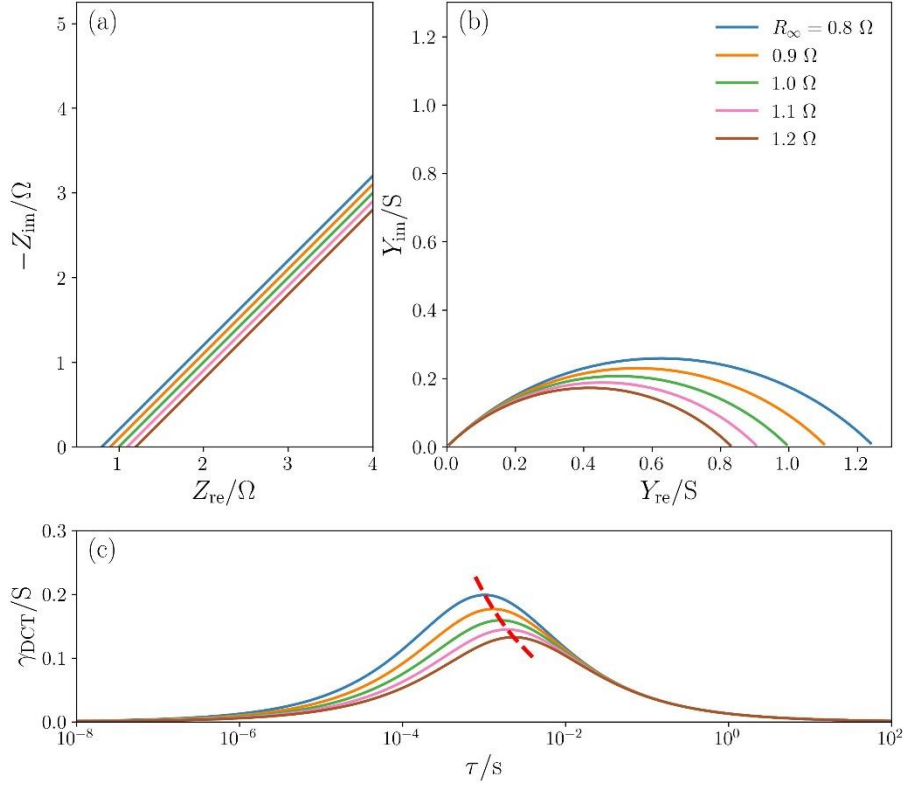


Figure 2. Nyquist plots of the (a) impedance and (b) admittance, and (c) DCT for the generalized Warburg element at various  $R_\infty$  values.

### 5.1.2 ZARC Element

The DRT and DCT can also be compared for the ZARC element (Section 2.2). The values of the specific circuit parameters used are given in Table S3 of SI2. Panels (a), (b), (c), and (d) of Figure 3 show the impedance, admittance, DRT, and DCT for different values of  $R_{ct}$ , respectively. On the one hand, increasing  $R_{ct}$  monotonically increases the height and area of the DRT peak, see Figure 3 (c). On the other hand, an increase in  $R_{ct}$  results in a decrease of the position,  $\log \tau_{ZARC-DCT}$ , of the DCT peak, while the height,  $\frac{R_{ct}}{2\pi R_\infty(R_\infty + R_{ct})} \tan\left(\frac{\pi\phi}{2}\right)$ , and area,  $\frac{R_{ct}}{R_\infty(R_\infty + R_{ct})}$ , monotonically increase (Figure 3 (d)). This highlights one major difference between the DRT and the DCT.

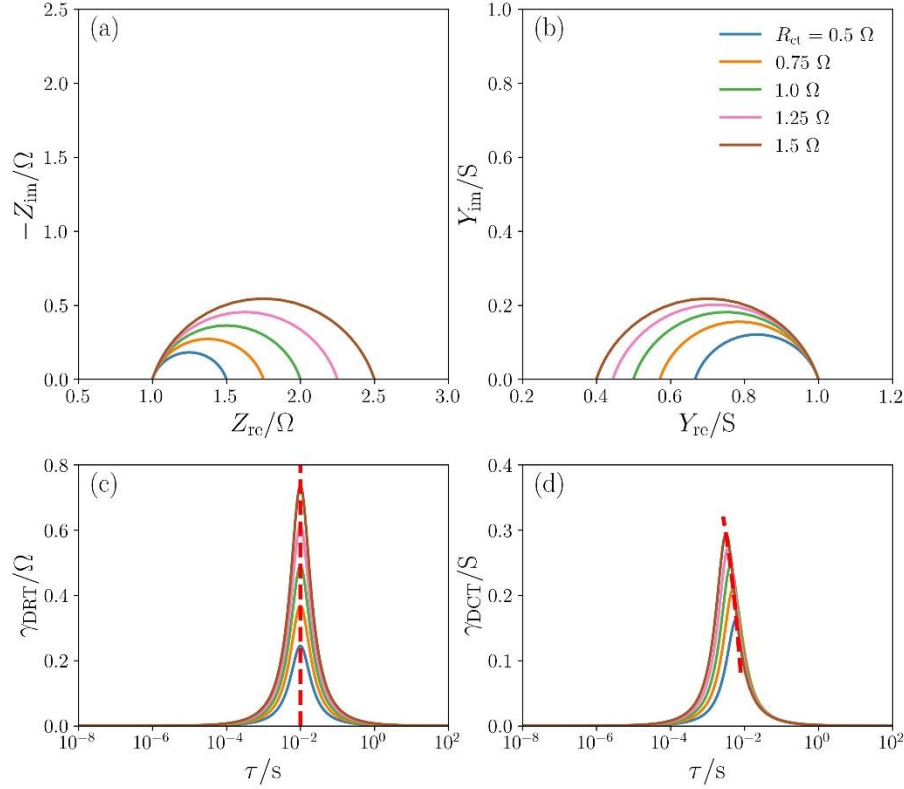


Figure 3. Nyquist plots of the (a) impedance and (b) admittance, (c) DRT, and (d) DCT for the ZARC element at various  $R_{ct}$  values.

We also varied the resistance  $R_{\infty}$  as shown in Figure 4 to highlight another major difference between the DRT and the DCT. While the DRT peak is not impacted by a change in  $R_{\infty}$  (Figure 4 (c) and (10)), the position, height, and area of the DCT peak vary with  $R_{\infty}$  (Figure 4 (d)): the peak position monotonically increases with  $R_{\infty}$  whereas the peak height and area monotonically decrease as  $R_{\infty}$  increases. This implies that the DRT can be used to determine  $\tau_{ZARC}$ ,  $R_{ct}$ , and  $\phi$ , but not the resistance  $R_{\infty}$ , which can only be evaluated using the DCT.

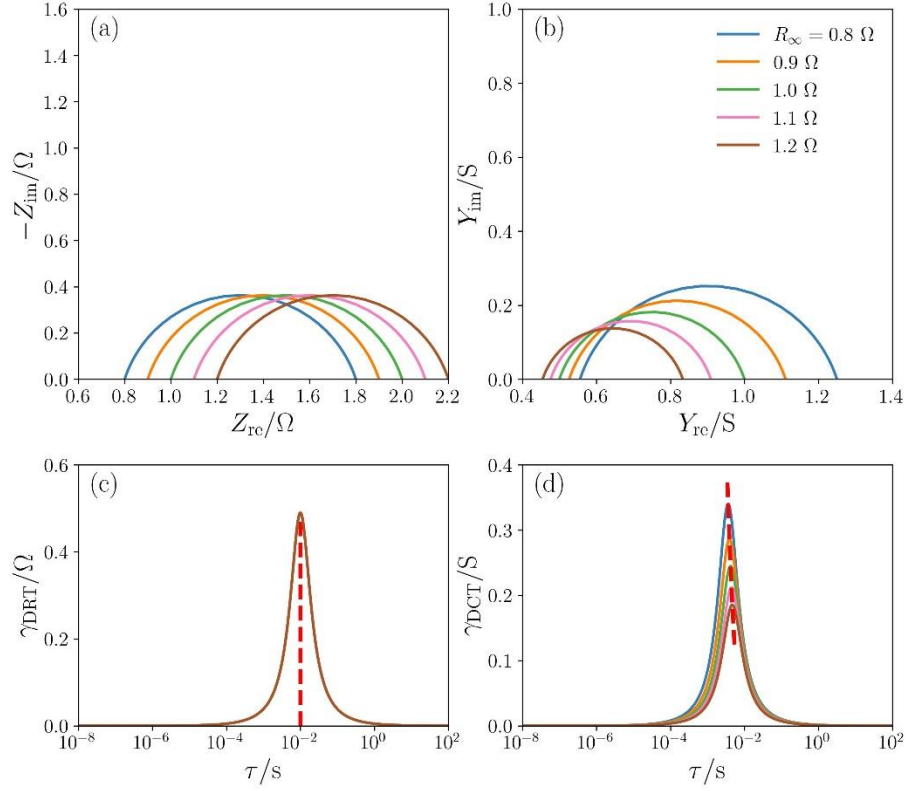


Figure 4. Nyquist plots of the (a) impedance and (b) admittance, (c) DRT, and (d) DCT for the ZARC element at various  $R_\infty$  values.

### 5.1.3 ZARC + Generalized Warburg

Panels (a), (b), and (c) of Figure 5 show the impedance, admittance, and DCT for various values of  $R_{\text{ct}}$ , respectively, for the series combination of a ZARC element and a generalized Warburg element (Section 2.3).

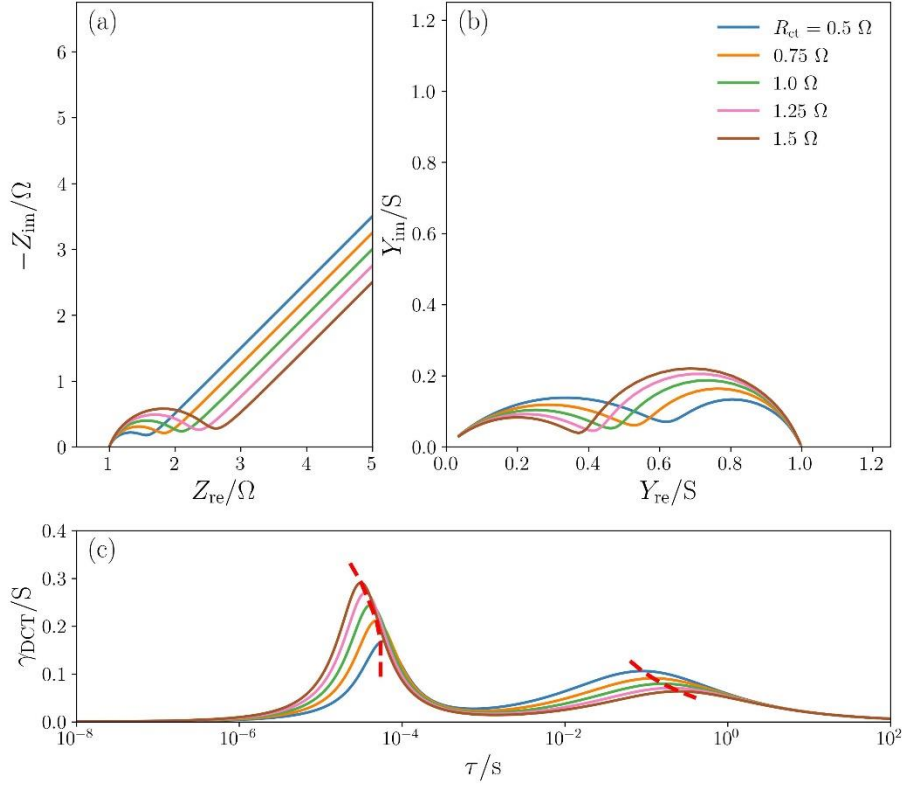


Figure 5. Nyquist plots of the (a) impedance and (b) admittance, and (c) DCT for the series combination of a ZARC element and a generalized Warburg element at various  $R_{ct}$  values.

Similar plots obtained by varying the resistance  $R_{\infty}$  and the Warburg coefficient  $A$  are shown in Figures S3 and S4 of SI2, respectively. The values of the specific circuit parameters used are given in Table S4 of SI2. We note that the DCT spectra exhibit one peak for each semi-circle in the Nyquist plots of the admittance, see Figure S5 of SI2. For the low-frequency peak, increasing  $R_{ct}$  or  $R_{\infty}$  shifts the peak position,  $\log \tau_{W-DCT}$ , to higher timescales and decreases the peak height,  $\frac{1}{2\pi(R_{\infty}+R_{ct})} \tan\left(\frac{\pi\alpha}{2}\right)$ , and area,  $\frac{1}{R_{\infty}+R_{ct}}$  (Figure 5 (c) and Figure S3 (c)). For the high-frequency peak, rising  $R_{ct}$  shifts the peak position,  $\log \tau_{ZARC-DCT}$ , to lower timescales and increases the peak height,  $\frac{R_{ct}}{2\pi R_{\infty}(R_{\infty}+R_{ct})} \tan\left(\frac{\pi\phi}{2}\right)$ , and area,  $\frac{R_{ct}}{R_{\infty}(R_{\infty}+R_{ct})}$  (Figure 5 (c)). Moreover, augmenting  $R_{\infty}$  increases  $\log \tau_{ZARC-DCT}$  and decreases the height and area of the high-frequency peak (Figure S3 (c) of SI2). Additionally, the Warburg coefficient  $A$  only affects  $\log \tau_{W-DCT}$ , which monotonically decreases as  $A$  increases (Figure S4 (c) of SI2). We

stress that the position,  $\log \tau_{W-DCT}$ , of the low-frequency peak is shifted and depends on both  $R_\infty$  and  $R_{ct}$ . Moreover, Figures S5, S6, and S7 of SI2 show the impedance, admittance, and DCT for different values of  $R_{ct}$ ,  $R_\infty$ , and  $A$ , respectively for the series association of a HN element and a generalized Warburg element. The values of the circuit parameters used are reported in Table S4 of SI2. We observe that  $R_{ct}$ ,  $R_\infty$ , and  $A$  affect the position, height, and area of the two DCT peaks of the HN + generalized Warburg association in the same way as they do for the ZARC + generalized Warburg combination.

### 5.1.4 YARC Element

Panels (a), (b), (c), and (d) of Figure 6 show the impedance, admittance, DRT, and DCT plots for different values of  $G_{ct}$  for the YARC element, respectively (Section 2.4).

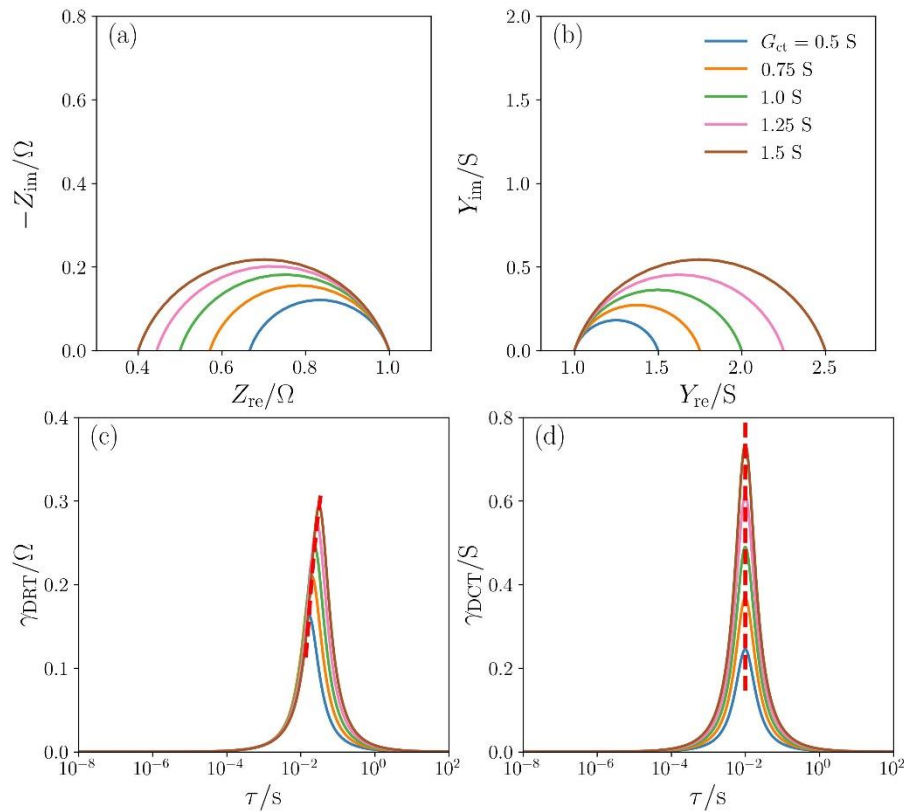


Figure 6. Nyquist plots of the (a) impedance and (b) admittance, and (c) DRT and (d) DCT for the YARC element at various  $G_{ct}$  values.

Similar plots are shown for the double YARC model in Figure S8 of SI2. The values of the circuit parameters are reported in Table S5 of SI2. Consistent with (9) and (21), the YARC impedance, admittance, DRT, and DCT correspond to the ZARC admittance, impedance, DCT, and DRT, respectively, see Figure 3, Figure 4, and Figure 6.

## 5.2 Analysis of Artificial and Real Battery Data

### 5.2.1 Artificial Experiments

We first used artificial EIS data to investigate the robustness of the DNN-based deconvolution of the DCT when the exact impedance, the exact DCT, and the experimental noise are known.

#### 5.2.1.1 Double ZARC + Generalized Warburg

We start our analysis with the series combination of a double ZARC element and a generalized Warburg element (Section 2.3), whose exact impedance is given by [25]

$$Z(f; R_\infty, \mathbf{R}_{ct}, \boldsymbol{\tau}_{ZARC}, \boldsymbol{\phi}, A, \alpha) \quad (31)$$

$$= R_\infty + \frac{R_{ct,1}}{1 + (i2\pi f \tau_{ZARC,1})^{\phi_1}} + \frac{R_{ct,2}}{1 + (i2\pi f \tau_{ZARC,2})^{\phi_2}} + \frac{A}{(i2\pi f)^\alpha}$$

The exact DCT is obtained by setting  $K=3$ ,  $\psi_1 = \psi_2 = \psi_3 = 1$ , and  $P = 1$  in (20b). Using the values of the parameters reported in Table S6 of SI2, we generated experimental data by adding white noise,  $\varepsilon(f)$ , to  $Z(f; R_\infty, \mathbf{R}_{ct}, \boldsymbol{\tau}_{ZARC}, \boldsymbol{\phi}, A, \alpha)$ , see (30) with  $\sigma_n^{\text{exp}} = 5.00 \times 10^{-1} \Omega$ . The frequencies ranged from  $10^{-3}$  Hz to  $10^6$  Hz with 10 points per decade. Panels (a) and (b) of Figure 7 show the Nyquist plots of the exact, “experimental”, and regressed impedances and admittances, respectively.

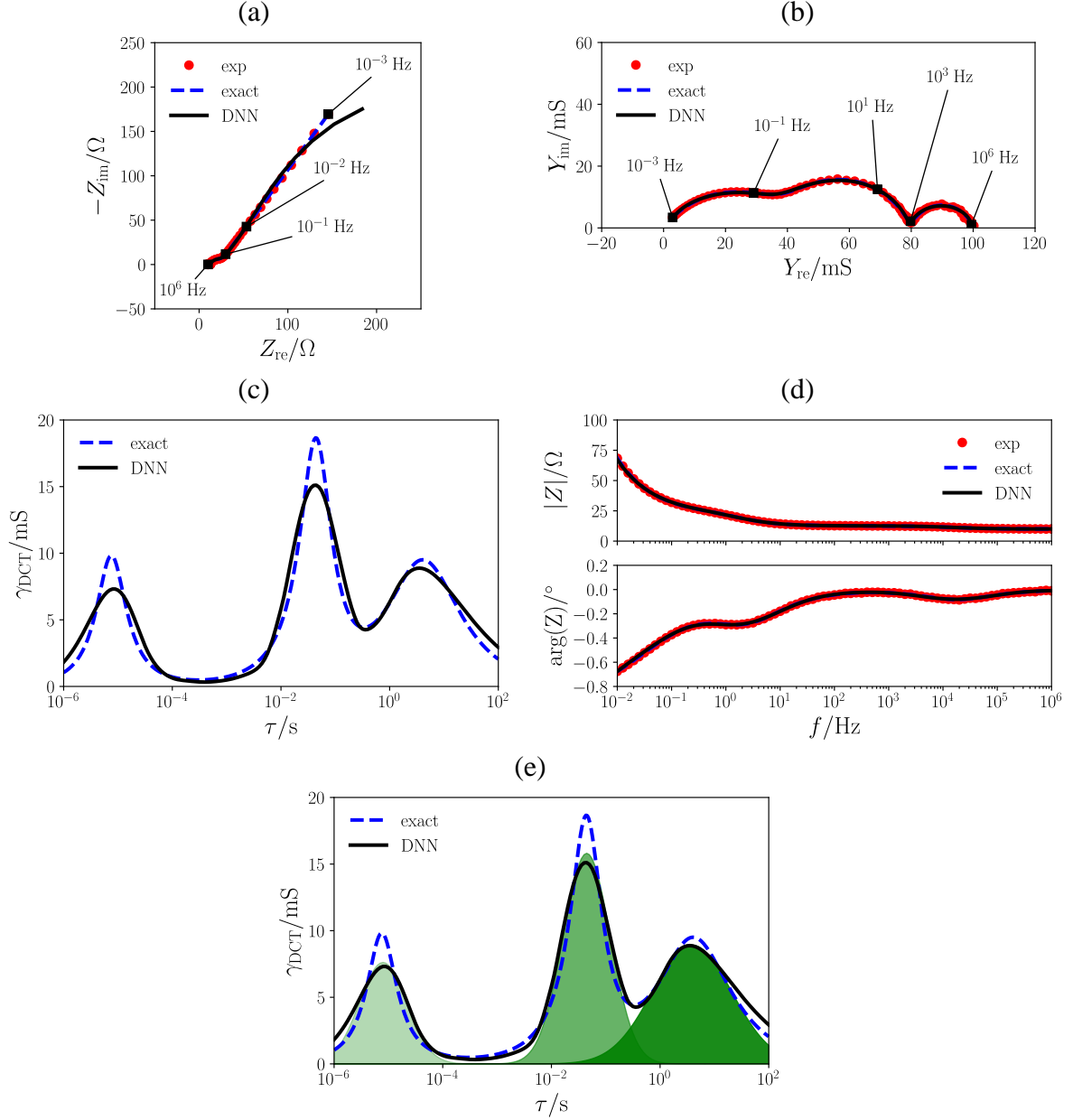


Figure 7. Nyquist plots of the exact, “experimental”, and regressed (a) impedances and (b) admittances for the series combination of a double ZARC element and a generalized Warburg element. The exact and regressed DCTs are shown in panel (c), the Bode plots of the exact, “experimental”, and regressed impedances are given in panel (d), and the separated DCT peaks are shown in panel (e).

Next, we used the DNNs described in Section 3 to deconvolve the DCT, which is shown in Figure 7 (c) with the exact DCT. We note that the exact DCT was accurately recovered, which is consistent with the residuals between the “experimental” and estimated admittances that



converge after approximately  $4.00 \times 10^4$  iterations (Figure S9 (a) of SI2). Moreover, we used a modified version of the peak-separation algorithm of pyDRTtools based on (28) to separate the peak of the DNN-regressed DCT (Section 3). The peak separation enabled us to identify the

characteristic timescales  $\tau_{\text{ZARC-DCT},1} = \tau_{\text{ZARC},1} \left( \frac{R_\infty}{R_\infty + R_{\text{ct},1}} \right)^{\frac{1}{\phi_1}}$ ,  $\tau_{\text{ZARC-DCT},2} = \tau_{\text{ZARC},2} \left( \frac{R_\infty}{R_\infty + R_{\text{ct},2}} \right)^{\frac{1}{\phi_2}}$ , and  $\tau_{\text{W-DCT}} = \left( \frac{R_\infty + R_{\text{ct},1} + R_{\text{ct},2}}{A} \right)^{\frac{1}{\alpha}}$ , see the red dashed lines in Figure 7 (c).

The interpretation of these timescales is discussed in Section 5.2.1.3. Next, we recovered the admittance using (28) from the regressed DCT, before we recovered the impedance as the inverse of the estimated admittance. The Bode plots of the exact, “experimental”, and regressed impedances and admittances are shown in Figure 7 (d) and Figure S10 (a) of SI2, respectively. Notably, the exact impedance and admittance were closely regressed. However, we observed a slight mismatch between the exact and regressed impedances at low frequencies. Although the exact admittance was accurately regressed over the complete range of probed frequencies, this deviation arose from taking the inverse of the estimated admittances. In fact, applying the inverse intensifies the difference between regressed and “experimental” data. Another reason for this mismatch at low frequencies stems from the experimental noise, which usually affects the impedance more at low frequencies.

### 5.2.1.2 De Levie’s Model

We also generated artificial data based on de Levie’s model (Section 2.5) by adding white noise to the de Levie impedance given in (25). We first varied the ionic resistance,  $R_{\text{ion}}$ , with  $\sigma_n^{\text{exp}} = 1.00 \times 10^{-1} \Omega$ , before we varied the resistance  $R_\infty$  with  $\sigma_n^{\text{exp}} = 2.00 \times 10^{-2} \Omega$ . The values of the parameters are reported in Table S7 of SI2. The frequencies ranged from  $10^{-3}$  Hz to  $10^6$  Hz with 10 points per decade. For illustrative purposes, panels (a) and (b) of Figure 8 show the Nyquist plots of the exact, “experimental”, and regressed impedances and admittances for  $R_{\text{ion}} = 2.00 \times 10^1 \Omega$  and  $R_\infty = 1.00 \times 10^1 \Omega$ , respectively. Using the two DNNs described in

Section 3, we deconvolved the DCT, and recovered the exact admittance using (28). Then, we recovered the impedance as the inverse of the estimated admittance. The exact and regressed DCTs are shown in Figure 8 (c) and in panel (a) of Figures S11-S19 of SI2.

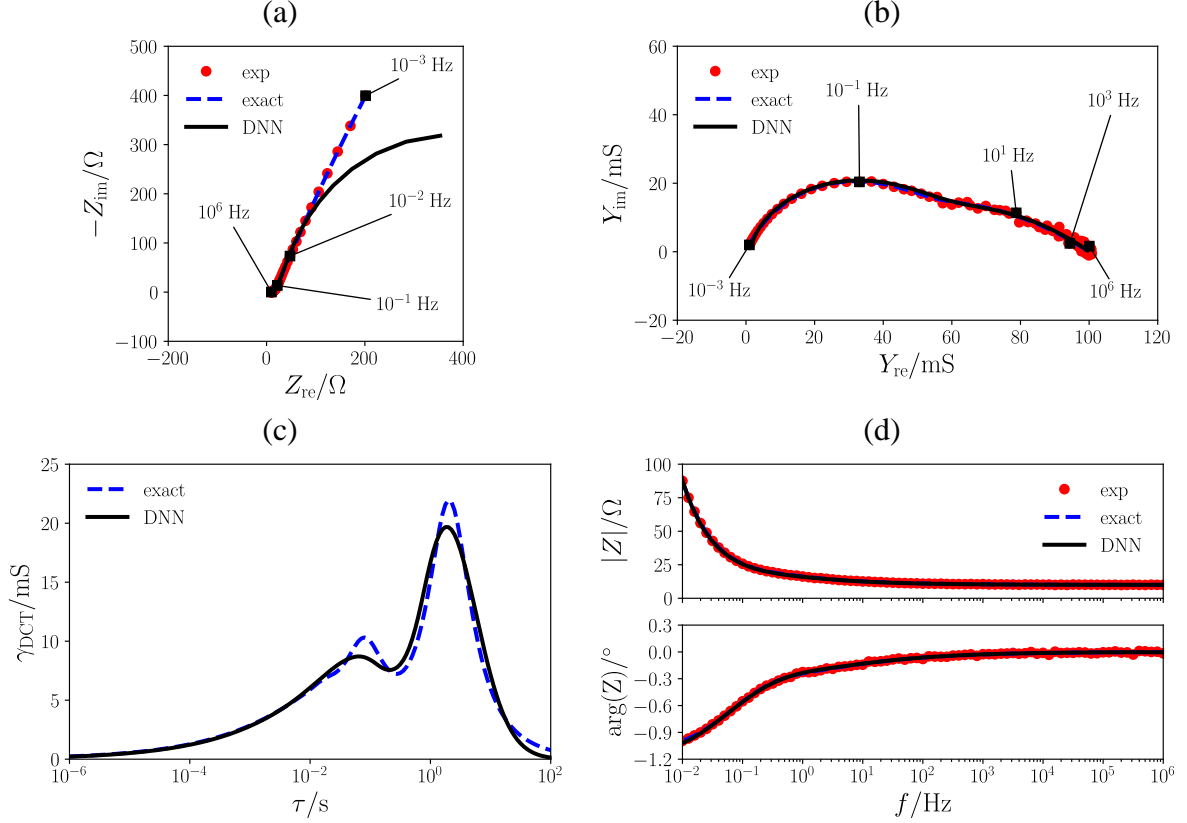


Figure 8. Nyquist plots of the exact, “experimental”, and regressed (a) impedances and (b) admittances for de Levie’s model ( $R_{ion} = 2.00 \times 10^1 \Omega$  and  $R_{\infty} = 1.00 \times 10^1 \Omega$ ). The exact and regressed DCTs are shown in panel (c), and the Bode plots of the exact, “experimental”, and regressed impedances are given in panel (d).

The exact DCTs were accurately regressed (Figure 8 (c) and panel (a) of Figures S11-S19 of SI2), which is consistent with the convergence of the admittance residuals shown in panels (b) and (c) of Figure S9 of SI2. The accurate DCT recovery led to the precise recovery of the exact admittances, as evidenced by the Bode plots of the exact, “experimental”, and estimated admittances shown in panel (b) of Figure S10 and Figures S11-S19 of SI2. The exact impedances were also accurately regressed, see the Bode plots in panel (c) of Figure 8 and

Figures S11-S19 of SI2. Lastly, panels (a) and (c) of Figure 9 show the waterfall plots of the recovered DCTs obtained for various values of  $R_{\text{ion}}$  and  $R_{\infty}$ , respectively. The corresponding contour plots are shown in panels (b) and (d) of Figure 9. We observed that  $R_{\text{ion}}$  was responsible for the apparition of one peak around  $\sim 1.00 \times 10^0$  s in the DCT spectrum, while  $R_{\infty}$  led to the appearance of two peaks at  $\sim 1.00 \times 10^{-1}$  s and  $1.00 \times 10^0$  s. We stress that these observations could not be made with the DRT method.

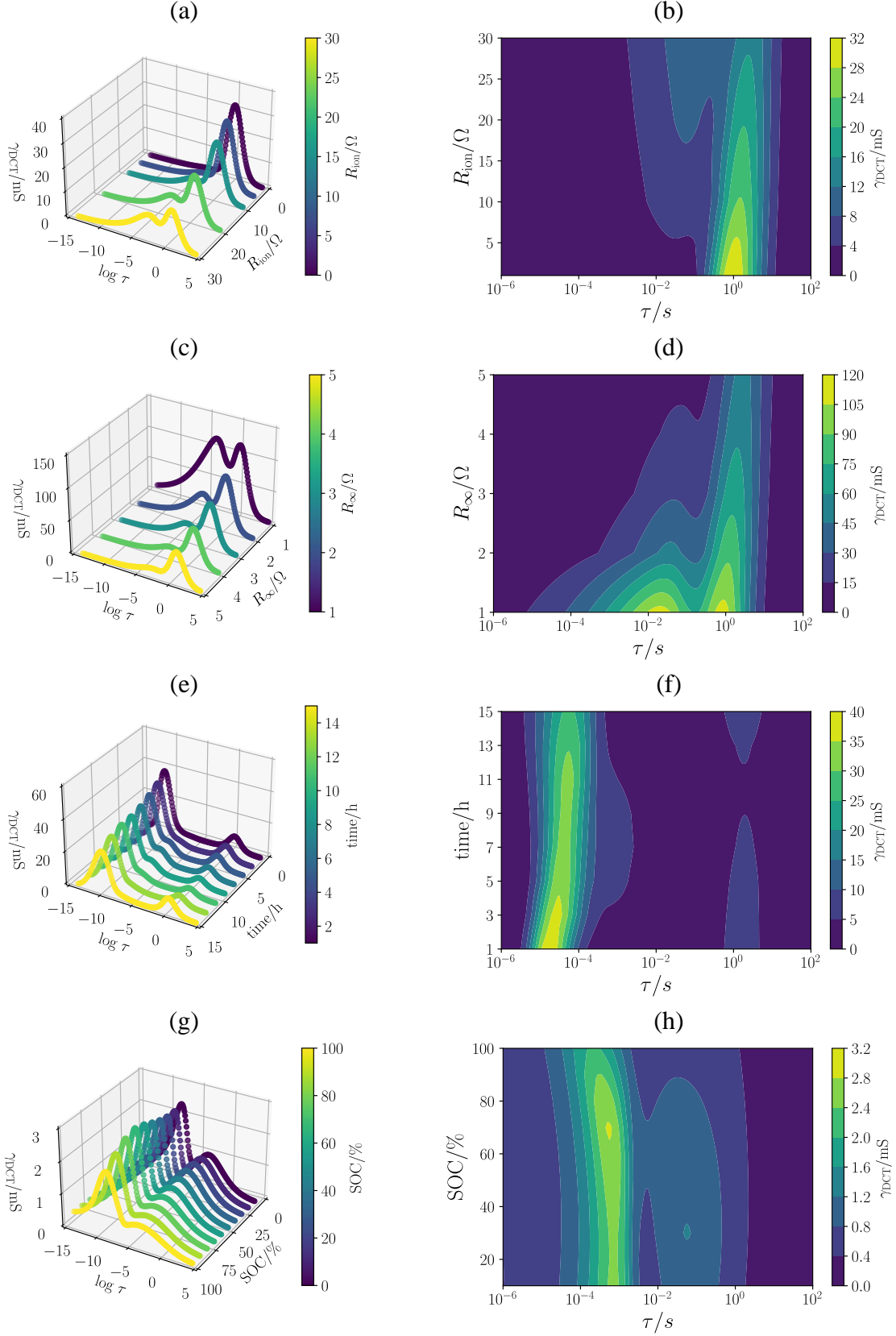


Figure 9. Waterfall plots of the recovered DCTs for de Levie model with varying (a)  $R_{ion}$  and (c)  $R_{\infty}$ , and for the (e)  $LiO_2$  and (g) ML621 batteries. The corresponding contour plots are shown in panels (b), (d), (f), and (h).

### 5.2.1.3 ZARC + Generalized Warburg

In this section, we illustrate how the DCT can be used to estimate physical parameters. We first generated 100 spectra using the exact impedance of the series combination of a ZARC element and a generalized Warburg element (Section 2.3) like we did in Sections 5.2.1.1 and 5.2.1.2. The values of the parameters used are given in Table 1.

Table 1 – Exact and estimated values of the parameters of the series combination of a ZARC element and a generalized Warburg element.

Parameter	Exact value	Estimate
$R_{\infty} [\Omega]$	$1.00 \times 10^0$	$1.05 \times 10^0 \pm 2.09 \times 10^{-3}$
$R_{ct} [\Omega]$	$1.00 \times 10^0$	$1.08 \times 10^0 \pm 8.56 \times 10^{-4}$
$\phi [-]$	$8.00 \times 10^{-1}$	$7.61 \times 10^{-1} \pm 3.49 \times 10^{-3}$
$\alpha [-]$	$6.00 \times 10^{-1}$	$5.97 \times 10^{-1} \pm 1.30 \times 10^{-3}$
$\tau_{ZARC} [s]$	$1.00 \times 10^{-4}$	$1.05 \times 10^{-4} \pm 7.55 \times 10^{-7}$
$A [\Omega \cdot s^{-\alpha}]$	$2.50 \times 10^0$	$2.66 \times 10^0 \pm 7.14 \times 10^{-3}$

Panels (a) and (b) of Figure 10 show the Nyquist plots of the exact, “experimental”, and regressed impedances and admittances, respectively.

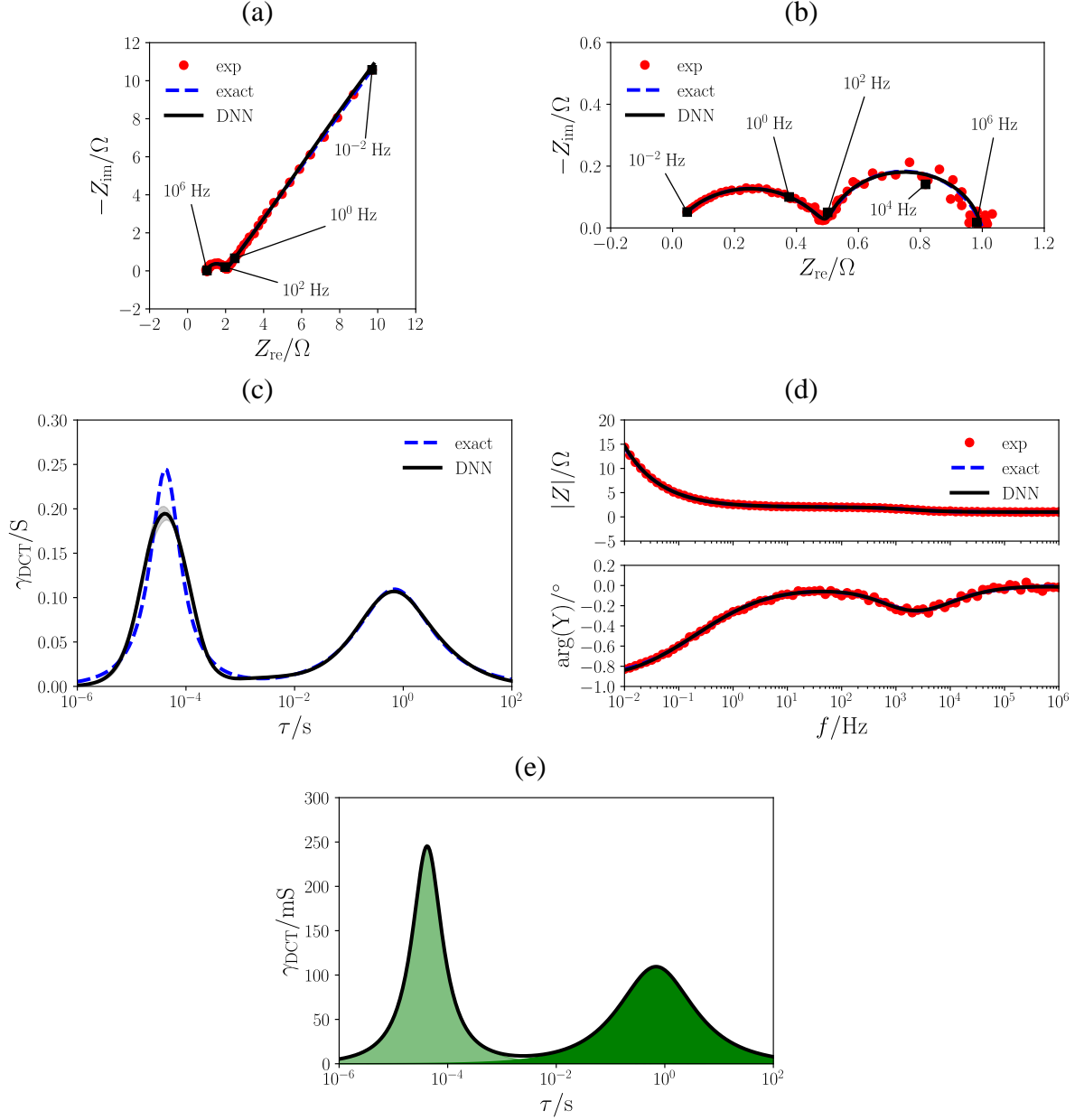


Figure 10. Nyquist plots of the exact, “experimental”, and regressed (a) impedances and (b) admittances for the series combination of a ZARC element and a generalized Warburg element. The exact and regressed DCTs are shown in panel (c), the Bode plots of the exact, “experimental”, and regressed impedances are given in panel (d), and the separated DCT peaks are shown in panel (e).

Next, we used the DNNs described in Section 3 to deconvolve the DCT (Figure S20 of SI2). Using the 100 deconvolved DCTs, we computed the mean and standard deviation DCTs. The mean and  $3\times$  credible bands of the regressed DCTs are shown as a black line and gray regions

in Figure 10 (c), respectively. Both peaks of the exact DCT can be distinguished, and the corresponding characteristic timescales,  $\tau_{\text{ZARC-DCT}} = \tau_{\text{ZARC}} \left( \frac{R_{\infty}}{R_{\infty} + R_{\text{ct}}} \right)^{\frac{1}{\phi}}$  and  $\tau_{\text{W-DCT}} = \left( \frac{R_{\infty} + R_{\text{ct}}}{A} \right)^{\frac{1}{\alpha}}$ , see (19) in Section 2.2, were identified. Then, the admittances were computed using (28) from the regressed DCTs. Next, we recovered the impedances as the inverse of the estimated admittances. Overall, the obtained residuals (Figure 10 (d), and Figure S9 (d) and Figure S10 (c) of SI2) indicate accurate recovery. We also separated each peak using the procedure described in Section 5.2.1.1. Having separated each peak, we followed the procedure outlined in Section 1.6 of SI1 to estimate the parameters  $R_{\infty}$ ,  $R_{\text{ct}}$ ,  $\phi$ ,  $\alpha$ ,  $\tau_{\text{ZARC}}$ , and  $A$ . The estimated values of these parameters are compared in Table 1 and Figure S21 (a) of SI2, which indicate accurate albeit biased recovery.

We also tested if this approach works well for estimating characteristic parameters when  $\varepsilon(f)$  given in (30) is proportional to the modulus of the exact impedance [45,46], *i.e.*,

$$\varepsilon(f) = \sigma_n^{\text{exp}} |Z_{\text{exact}}(f)| \quad (32)$$

with  $\sigma_n^{\text{exp}} = 2.00 \times 10^{-1}$ .

The mean and  $3 \times$  credible bands of the recovered DCT are shown in Figures S22 and S23 (a) of SI2; the Bode plots of the exact, “experimental”, and regressed impedances and admittances are shown in panels (b) and (c) of Figure S23 of SI2, respectively. The results show that the exact DCT, admittance, and impedance were all closely recovered (Figure S9 (e) and Figure S23 of SI2), and the circuit parameters were accurately estimated (Table S8 and Figure S21 (b) of SI2).

### 5.2.2 Real Experiments

To test the approach, we also used real data from two lithium batteries.

### 5.2.2.1 Lithium-oxygen Battery

We first considered EIS data from a LiO<sub>2</sub> battery [47]. The EIS frequencies spanned from 10 mHz to 100 kHz with six points per decade for the potentiostatic EIS measurements at various discharge times. Panels (a) and (b) of Figure 11 show the Nyquist plots of the experimental impedances and admittances, respectively, at the seven-th hour. Subsequent times were also analyzed, as shown in Figures S24-S30 of SI2.

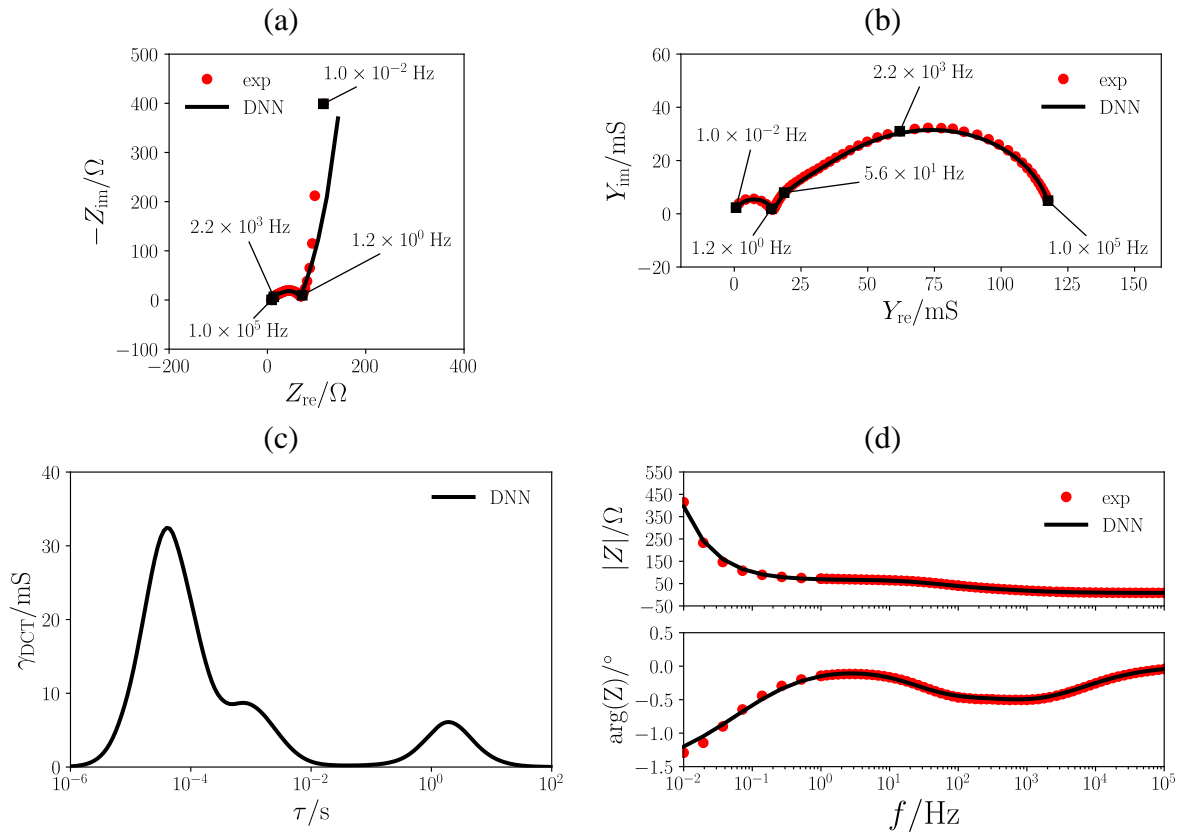


Figure 11. For the LiO<sub>2</sub> battery at  $t=7\text{h}$ , Nyquist plots of the experimental and regressed (a) impedances and (b) admittances, (c) regressed DCT, and (d) Bode plots of the experimental and regressed impedances.

We used the DNNs described in Section 3 to deconvolve the DCTs, which are shown in Figure 11 (c) and Figures S24-S30 (a) of SI2, while the waterfall and contour plots of the regressed DCTs are shown in panels (e) and (f) of Figure 9. These plots facilitate the assessment of the discharge's impact on the DCT. As explained in [47], the peak at  $\tau \approx 10^{-5} \text{ s}$  is assigned to the



contact resistance, while the peak at  $\tau \approx 10^{-6}$  s is related to the diffusion of  $O_2$  through the composite electrode. We also estimated the admittances using (28) to compute the impedances as the inverse of the estimated admittances. The admittance residuals are given in Figure S9 (f), and the Bode plots are shown in Figure 11 (d), Figure S10 (d), and panels (b) and (c) of Figures S24-S30 of SI2.

### 5.2.2.2 Rechargeable $LiMnO_2$ -based Lithium Battery

We also analyzed EIS data from a commercial  $LiMnO_2$  rechargeable battery (Panasonic ML621) at the states of charge (SOC) of 10%, 20%, ..., and 100%. The battery was charged at a constant current of 0.1 mA until a voltage of 3.1 V was reached. After a two-minute rest, a constant voltage charge at 3.1 V was carried out until the current decayed to 0.001 mA. To discharge the battery in steps of 10% SOC, a constant discharge current of 0.1 mA was imposed for five hours until 0.5 mAh of the battery's nominal 5 mAh capacity had been discharged. A lower voltage cutoff of 2.0 V was applied for safety. The EIS frequencies were taken between 7.0 MHz and 1.0 Hz with 20 points per decade. The results of the Kramers-Kronig tests are shown in Figures S31 and S32 of SI2 [22,38,48], indicating limited Kramers-Kronig compliance at high frequencies. For illustrative purposes, the Nyquist plots of the experimental and recovered impedances and admittances for SOC=10% are shown in panels (a) and (b) of Figure 12, respectively. The admittance spectra exhibited two separated arcs, see Figure 12 (b), which suggests that (19) can be used to model the DCT of these EIS spectra. We used the procedure described in Sections 5.2.1 and 5.2.2.1 to deconvolve the DCTs and estimate the admittances and impedances. The recovered DCTs for SOC=10%, 20%, ..., and 100% are shown in Figure 12 (c) and in panel (a) of Figures S33-S41 of SI2, respectively.

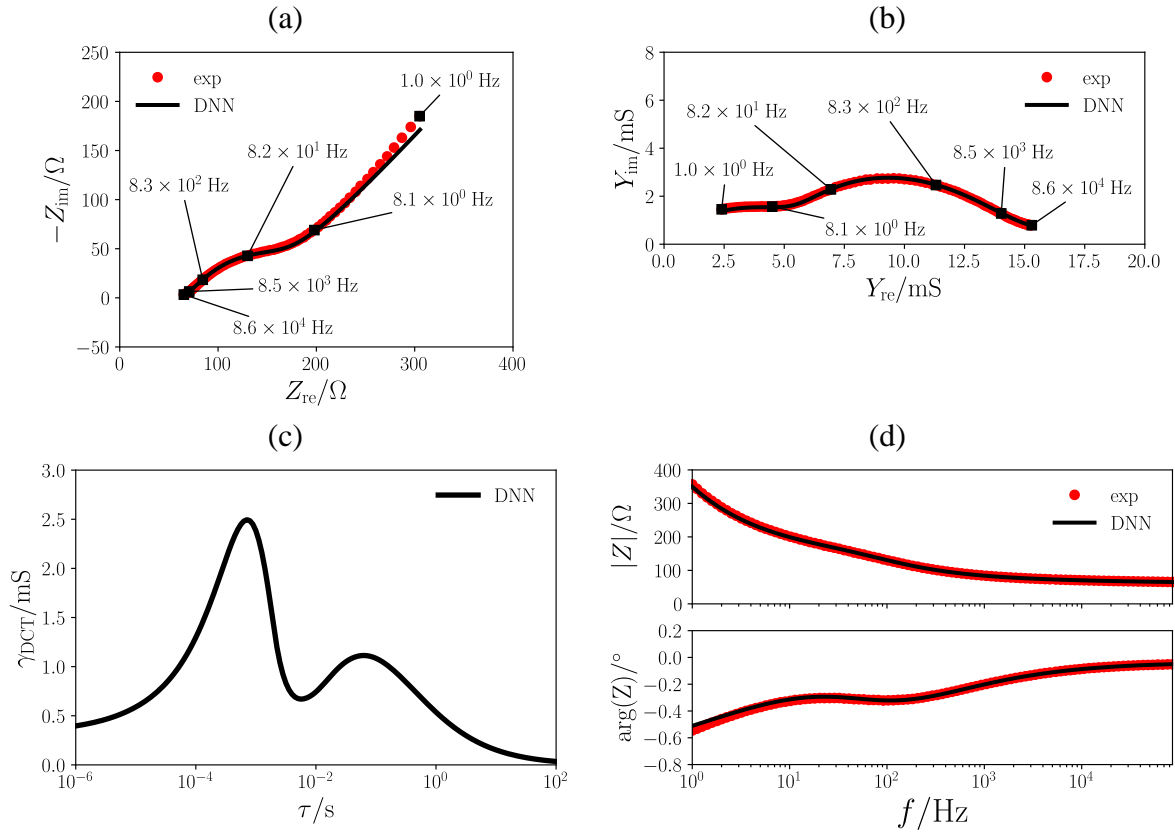


Figure 12. For the ML621 battery at 10% SOC, Nyquist plots of the experimental and regressed (a) impedances and (b) admittances, (c) regressed DCT, and (d) Bode plots of the experimental and regressed impedances.

The DCT enabled us to identify the timescales  $\tau_{ZARC-DCT} \approx 1.0$  ms and  $\tau_{W-DCT} \approx 0.1$  s related to charge-transfer and diffusional phenomena, respectively, see panels (g) and (h) of Figure 9 (h). The admittances and impedances were also estimated. The admittance residuals are shown in Figure S9 (g), while the Bode plots are reported in Figure 12 (d), Figure S10 (e), and panels (b) and (c) of Figures S33-S41 of SI2.

## 6 Conclusions

Although the DRT method holds significant potential for the analysis of EIS spectra, its asymptotic behavior at low frequencies is not congruent with that of electrochemical systems with blocking electrodes, such as batteries and supercapacitors. In such systems, the DRT method is asymptotically consistent only at intermediated and high frequencies. The DCT

method, which uses the admittance instead of the impedance, can overcome this challenge. However, the DCT is still not well established. Therefore, several DCT-specific analytical formulae are first derived herein. These formulae allow the comparison of DCT and DRT peak characteristics (position, width, and height). Additionally, deep neural networks were used to analyze EIS data through the lens of the DCT. This approach, validated on both artificial and real EIS data, underscores the usefulness of the DCT method for battery data analysis. This work enhances the scope of non-parametric models, hence paving the way for broader data interpretation.

### **Code Availability**

Relevant code is available at <https://github.com/ciuccislab/pyDRTtools> and <https://github.com/ciuccislab/EIS-DCT>.

### **Author Credit Statement**

Baptiste Py: Software Extension, Software Validation, Conceptualization, Methodology, Theory Development, Data Curation, Formal Analysis, Investigation, Writing – Original Draft, Writing – Review & Editing. Adeleke Maradesa: Software Extension, Experimental Investigation, Review. Francesco Ciucci: Software Creation, Software Development, Software Validation, Conceptualization, Methodology, Theory Development, Investigation, Resources, Review & Editing, Funding Acquisition, Project Administration, Supervision.

### **Declaration of Competing Interest**

None.

### **Acknowledgments**

The authors gratefully acknowledge the financial support from the Research Grants Council of Hong Kong (RGC Ref No. 16201820 and 16206019). This work was supported in part by the Project of Hetao Shenzhen-Hong Kong Science and Technology Innovation Cooperation Zone (HZQB-KCZYB-2020083). B. Py and A. Maradesa kindly thank the Hong Kong PhD. Fellowship Scheme for its financial support. Lastly, B. Py and A. Maradesa are grateful to Matthew James Robson for technical support with the cycling and EIS experiments related to the ML621 battery.

### **Declaration of Generative AI in the Writing Process**

While drafting this manuscript, the authors employed ChatGPT to assist in rephrasing certain sections so that readability could be enhanced. After utilizing this tool, the authors reviewed, revised, and rewrote the text.

## **List of Symbols**

### **Greek letters**

$\psi$	Vector of experimental conditions
$\alpha$	Warburg exponent
$\gamma_{\text{DCT}}$	Distribution of capacitive times
$\gamma_{\text{DRT}}$	Distribution of relaxation times
$\varepsilon$	Experimental noise for the synthetic experiments

$\sigma_n^{\text{exp}}$	Standard deviation of the experimental noise for the synthetic experiments
$\tau, \tau_0$	Timescales
$\tau_{\text{HN}}$	Characteristic timescale for the HN impedance
$\tau_{\text{YARC}}$	Characteristic timescale for the YARC admittance
$\tau_{\text{ZARC}}$	Characteristic timescale for the ZARC impedance
$\tau_{\text{W-DCT}}$	Characteristic timescale of the DCT of the generalized Warburg element
$\tau_{\text{ZARC-DCT}}$	Characteristic timescale of the DCT of the ZARC element
$\phi$	Dispersion factor
$\psi$	Symmetry parameter

### Greek letters

$A$	Warburg coefficient
$f$	Frequency
$\text{FWHM}_{\log \tau}$	Full-width-at-half-maximum
$G_{\text{ct}}, G_0, G_{\infty}$	Conductances
$R_{\text{ct}}, R_{\text{ion}}, R_{\infty}$	Resistances
$R_{\text{ZARC-DCT}}$	Resistance $\frac{R_{\infty}(R_{\infty}+R_{\text{ct}})}{R_{\text{ct}}}$

$Y$	Admittance
$Z$	Impedance

## List of Symbols

DCT	Distribution of capacitive times
DNN	Deep neural network
DRT	Distribution of relaxation times
EIS	Electrochemical impedance spectroscopy
HN	Havriliak-Negami
SOC	State-of-charge

## References

- [1] B.Y. Chang, S.M. Park, Electrochemical impedance spectroscopy, *Annual Rev. Anal. Chem.* 3 (2010) 207–229.
- [2] E.K. Murphy, J. Skinner, M. Martucci, S.B. Rutkove, R.J. Halter, Toward electrical impedance tomography coupled ultrasound imaging for assessing muscle health, *IEEE Trans. Med. Imaging.* 38 (2019) 1409–1419.
- [3] K. Krukiewicz, Electrochemical impedance spectroscopy as a versatile tool for the characterization of neural tissue: A mini review, *Electrochem. Commun.* 116 (2020) 106742.
- [4] F. Ciucci, C. Chen, Analysis of electrochemical impedance spectroscopy data using the distribution of relaxation times: A Bayesian and hierarchical Bayesian approach, *Electrochim. Acta.* 167 (2015) 439–454.
- [5] O. Kanoun, A.Y. Kallel, H. Nouri, B.B. Atitallah, D. Haddad, Z. Hu, M. Talbi, A. Al-Hamry, R. Munja, F. Wendler, R. Barioul, T. Keutel, A. Mangler, Impedance spectroscopy: Applications, advances and future trends, *IEEE Instrum. Meas. Mag.* 25 (2022) 11–21.
- [6] J.G. Lyagaeva, G.K. Vdovin, D.A. Medvedev, Distinguishing bulk and grain boundary transport of a proton-conducting electrolyte by combining equivalent circuit scheme and distribution of relaxation times analyses, *J. Phys. Chem. C.* 123 (2019) 21993–21997.
- [7] D. Kim, E.S. Muckley, N. Creange, T.H. Wan, M.H. Ann, E. Quattrocchi, R.K. Vasudevan, J.H. Kim, F. Ciucci, I.N. Ivanov, S.V. Kalinin, M. Ahmadi, Exploring transport behavior in hybrid perovskites solar cells via machine learning analysis of environmental-dependent impedance spectroscopy, *Adv. Sci.* 8 (2021) 2002510.
- [8] M. Schönleber, E. Ivers-Tiffée, Approximability of impedance spectra by RC elements and implications for impedance analysis, *Electrochem. Commun.* 58 (2015) 15–19.

- [9] J. Liu, F. Ciucci, The Gaussian process distribution of relaxation times: A machine learning tool for the analysis and prediction of electrochemical impedance spectroscopy data, *Electrochim. Acta.* 331 (2020) 135316.
- [10] Y. Lu, C.Z. Zhao, J.-Q. Huang, Q. Zhang, The timescale identification decoupling complicated kinetic processes in lithium batteries, *Joule.* 6 (2022) 1172–1198.
- [11] E. Ivers-Tiffée, A. Weber, Evaluation of electrochemical impedance spectra by the distribution of relaxation times, *J. Ceram. Soc. Japan.* 125 (2017) 193–201.
- [12] L.E. Helseth, Modelling supercapacitors using a dynamic equivalent circuit with a distribution of relaxation times, *J. Energy Storage.* 25 (2019) 100912.
- [13] X. Li, M. Ahmadi, L. Collins, S.V. Kalinin, Deconvolving distribution of relaxation times, resistances and inductance from electrochemical impedance spectroscopy via statistical model selection: Exploiting structural-sparsity regularization and data-driven parameter tuning, *Electrochim. Acta.* 313 (2019) 570–583.
- [14] E. Barsoukov, J.R. Macdonald, *Impedance spectroscopy: Theory, experiment, and applications*, Third edition, Wiley, Hoboken, NJ, 2018.
- [15] F. Ciucci, Modeling electrochemical impedance spectroscopy, *Curr. Opin. Electrochem.* 13 (2019) 132–139.
- [16] A. Lasia, Modeling of impedance of porous electrodes, *Modern Aspects Electrochem.* (2009).
- [17] W. Lai, F. Ciucci, Mathematical modeling of porous battery electrodes — Revisit of Newman’s model, *Electrochim. Acta.* 56 (2011) 4369–4377.
- [18] A.Ch. Lazanas, M.I. Prodromidis, Electrochemical impedance spectroscopy — A tutorial, *ACS Meas. Sci. Au.* 3 (2023) 162–193.



- [19] G.J. Brug, A.L.G. Van Den Eeden, M. Sluyters-Rehbach, J.H. Sluyters, The analysis of electrode impedances complicated by the presence of a constant phase element, *J. Electroanal. Chem.* 176 (1984) 275–295.
- [20] A. Lasia, Electrochemical impedance spectroscopy and its applications, *Modern Aspects Electrochem.* (2002) 143–248.
- [21] B.A. Boukamp, A linear Kronig-Kramers transform test for immittance data validation, *J. Electrochem. Soc.* 142 (1995) 1885–1894.
- [22] F. Ciucci, The Gaussian process Hilbert transform (GP-HT): Testing the consistency of electrochemical impedance spectroscopy data, *J. Electrochem. Soc.* 167 (2020) 126503.
- [23] B.A. Boukamp, J.R. Macdonald, Alternatives to Kronig-Kramers transformation and testing, and estimation of distributions, *Solid State Ionics.* 74 (1994) 85–101.
- [24] A. Maradesa, B. Py, T.H. Wan, M.B. Effat, F. Ciucci, Selecting the regularization parameter in the distribution of relaxation times, *J. Electrochem. Soc.* 170 (2023) 030502.
- [25] A. Maradesa, B. Py, E. Quattrocchi, F. Ciucci, The probabilistic deconvolution of the distribution of relaxation times with finite Gaussian processes, *Electrochim. Acta.* 413 (2022) 140119.
- [26] E. Quattrocchi, B. Py, A. Maradesa, Q. Meyer, C. Zhao, F. Ciucci, Deconvolution of electrochemical impedance spectroscopy data using the deep-neural-network-enhanced distribution of relaxation times, *Electrochim. Acta.* 439 (2023) 141499.
- [27] B.A. Boukamp, Derivation of a distribution function of relaxation times for the (fractal) finite length Warburg., *Electrochim. Acta.* 252 (2017) 154–163.
- [28] J. Huang, M. Papac, R. O’Hayre, Towards robust autonomous impedance spectroscopy analysis: A calibrated hierarchical Bayesian approach for electrochemical impedance spectroscopy (EIS) inversion, *Electrochim. Acta.* 367 (2021) 137493.

- [29] Havriliak, S., Negami, S., A complex plane representation of dielectric and mechanical relaxation processes in some polymers, *Polymers*. 9 (1967) 161-210.
- [30] J. Xu, P. Gao, X. Qiu, H. Li, Q. Zhuang, K. Wu, H. Zheng, Kinetic and transport-characteristics of  $\text{LiNi}_{0.8}\text{Co}_{0.1}\text{Mn}_{0.1}\text{O}_2$  lithium-ion batteries, *Solid State Ionics*. 395 (2023) 116216.
- [31] R.M. Fuoss, J.G. Kirkwood, Electrical properties of solids. VIII. Dipole moments in polyvinyl chloride-diphenyl systems\*, *J. Am. Chem. Soc.* 63 (1941) 385–394.
- [32] U. Tröltzsch, O. Kanoun, H.-R. Tränkler, Characterizing aging effects of lithium ion batteries by impedance spectroscopy, *Electrochim. Acta*. 51 (2006) 1664–1672.
- [33] S.M. Gateman, O. Gharbi, H. Gomes De Melo, K. Ngo, M. Turmine, V. Vivier, On the use of a constant phase element (CPE) in electrochemistry, *Curr. Opin. Electrochem.* 36 (2022) 101133.
- [34] J. Liu, F. Ciucci, The deep-prior distribution of relaxation times, *J. Electrochem. Soc.* 167 (2020) 026506.
- [35] J. Huang, N.P. Sullivan, A. Zakutayev, R. O’Hayre, How reliable is distribution of relaxation times (DRT) analysis? A dual regression-classification perspective on DRT estimation, interpretation, and accuracy, *Electrochim. Acta*. 443 (2023) 141879.
- [36] J. Huang, Y. Gao, J. Luo, S. Wang, C. Li, S. Chen, J. Zhang, Editors’ choice — Review — Impedance response of porous electrodes: Theoretical framework, physical models and applications, *J. Electrochem. Soc.* 167 (2020) 166503.
- [37] R. Morasch, J. Keilhofer, H.A. Gasteiger, B. Suthar, Methods — Understanding porous electrode impedance and the implications for the impedance analysis of Li-Ion battery electrodes, *J. Electrochem. Soc.* 168 (2021) 080519.

- [38] T.H. Wan, M. Saccoccio, C. Chen, F. Ciucci, Influence of the discretization methods on the distribution of relaxation times deconvolution: Implementing radial basis functions with DRTtools, *Electrochim. Acta.* 184 (2015) 483–499.
- [39] K. Yang, J. Liu, Y. Wang, X. Shi, J. Wang, Q. Lu, F. Ciucci, Z. Yang, Machine-learning-assisted prediction of long-term performance degradation on solid oxide fuel cell cathodes induced by chromium poisoning, *J. Mater. Chem. A.* 10 (2022) 23683–23690.
- [40] X. Glorot, Y. Bengio, Understanding the difficulty of training deep feedforward neural networks, 13th Int. Conf. Artif. Intell. Statist. (2010) 249.
- [41] D.-A. Clevert, T. Unterthiner, S. Hochreiter, Fast and accurate deep network learning by exponential linear units (ELUs), (2016). <http://arxiv.org/abs/1511.07289>.
- [42] T. Szandala, Review and comparison of commonly used activation functions for deep neural networks, *Bio-inspired Neurocom.* (2021).
- [43] D.P. Kingma, J. Ba, Adam: A method for stochastic optimization, (2017). <http://arxiv.org/abs/1412.6980>.
- [44] B. Py, A. Maradesa, F. Ciucci, Gaussian processes for the analysis of electrochemical impedance spectroscopy data: Prediction, filtering, and active learning, *Electrochim. Acta.* 439 (2023) 141688.
- [45] P. Agarwal, M.E. Orazem, L.H. Garcia-Rubio, Application of measurement models to impedance spectroscopy: III . Evaluation of consistency with the Kramers-Kronig relations, *J. Electrochem. Soc.* 142 (1995) 4159–4168.
- [46] M.E. Orazem, P. Agarwal, C. Deslouis, B. Tribollet, Application of measurement models to electrohydrodynamic impedance spectroscopy, *J. Electrochem. Soc.* 143 (1996) 948–960.
- [47] J. Chen, E. Quattrocchi, F. Ciucci, Y. Chen, Charging processes in lithium-oxygen batteries unraveled through the lens of the distribution of relaxation times, *Chem.* (2023).

- [48] J. Liu, T.H. Wan, F. Ciucci, A Bayesian view on the Hilbert transform and the Kramers-Kronig transform of electrochemical impedance data: Probabilistic estimates and quality scores, *Electrochim. Acta.* 357 (2020) 136864.